arXiv:0812.2864v1 [hep-ex] 15 Dec 2008

DESY–08–178
December 2008

Subjet distributions in deep inelastic scattering at HERA

ZEUS Collaboration

Abstract

Subjet distributions were measured in neutral current deep inelastic ep scattering with the ZEUS detector at HERA using an integrated luminosity of 81.7 pb^{-1}. Jets were identified using the k_T cluster algorithm in the laboratory frame. Subjets were defined as jet-like substructures identified by a reapplication of the cluster algorithm at a smaller value of the resolution parameter $y_{\rm cut}$. Measurements of subjet distributions for jets with exactly two subjets for $y_{\rm cut} = 0.05$ are presented as functions of observables sensitive to the pattern of parton radiation and to the colour coherence between the initial and final states. Perturbative QCD predictions give an adequate description of the data.

The ZEUS Collaboration

S. Chekanov, M. Derrick, S. Magill, B. Musgrave, D. Nicholass[1], J. Repond, R. Yoshida
Argonne National Laboratory, Argonne, Illinois 60439-4815, USA [n]

M.C.K. Mattingly
Andrews University, Berrien Springs, Michigan 49104-0380, USA

P. Antonioli, G. Bari, L. Bellagamba, D. Boscherini, A. Bruni, G. Bruni, F. Cindolo, M. Corradi, G. Iacobucci, A. Margotti, R. Nania, A. Polini
INFN Bologna, Bologna, Italy [e]

S. Antonelli, M. Basile, M. Bindi, L. Cifarelli, A. Contin, S. De Pasquale[2], G. Sartorelli, A. Zichichi
University and INFN Bologna, Bologna, Italy [e]

D. Bartsch, I. Brock, H. Hartmann, E. Hilger, H.-P. Jakob, M. Jüngst, A.E. Nuncio-Quiroz, E. Paul, U. Samson, V. Schönberg, R. Shehzadi, M. Wlasenko
Physikalisches Institut der Universität Bonn, Bonn, Germany [b]

N.H. Brook, G.P. Heath, J.D. Morris
H.H. Wills Physics Laboratory, University of Bristol, Bristol, United Kingdom [m]

M. Kaur, P. Kaur[3], I. Singh[3]
Panjab University, Department of Physics, Chandigarh, India

M. Capua, S. Fazio, A. Mastroberardino, M. Schioppa, G. Susinno, E. Tassi
Calabria University, Physics Department and INFN, Cosenza, Italy [e]

J.Y. Kim
Chonnam National University, Kwangju, South Korea

Z.A. Ibrahim, F. Mohamad Idris, B. Kamaluddin, W.A.T. Wan Abdullah
Jabatan Fizik, Universiti Malaya, 50603 Kuala Lumpur, Malaysia [r]

Y. Ning, Z. Ren, F. Sciulli
Nevis Laboratories, Columbia University, Irvington on Hudson, New York 10027 [o]

J. Chwastowski, A. Eskreys, J. Figiel, A. Galas, K. Olkiewicz, B. Pawlik, P. Stopa, L. Zawiejski
The Henryk Niewodniczanski Institute of Nuclear Physics, Polish Academy of Sciences, Cracow, Poland [i]

L. Adamczyk, T. Bołd, I. Grabowska-Bołd, D. Kisielewska, J. Łukasik[4], M. Przybycień, L. Suszycki
Faculty of Physics and Applied Computer Science, AGH-University of Science and Technology, Cracow, Poland [p]

A. Kotański[5], W. Słomiński[6]
Department of Physics, Jagellonian University, Cracow, Poland

O. Behnke, U. Behrens, C. Blohm, A. Bonato, K. Borras, D. Bot, R. Ciesielski, N. Coppola, S. Fang, J. Fourletova[7], A. Geiser, P. Göttlicher[8], J. Grebenyuk, I. Gregor, T. Haas, W. Hain, A. Hüttmann, F. Januschek, B. Kahle, I.I. Katkov[9], U. Klein[10], U. Kötz, H. Kowalski, M. Lisovyi, E. Lobodzinska, B. Löhr, R. Mankel[11], I.-A. Melzer-Pellmann, S. Miglioranzi[12], A. Montanari, T. Namsoo, D. Notz[11], A. Parenti, L. Rinaldi[13], P. Roloff, I. Rubinsky, U. Schneekloth, A. Spiridonov[14], D. Szuba[15], J. Szuba[16], T. Theedt, J. Ukleja[17], G. Wolf, K. Wrona, A.G. Yagües Molina, C. Youngman, W. Zeuner[11]
Deutsches Elektronen-Synchrotron DESY, Hamburg, Germany

V. Drugakov, W. Lohmann, S. Schlenstedt
Deutsches Elektronen-Synchrotron DESY, Zeuthen, Germany

G. Barbagli, E. Gallo
INFN Florence, Florence, Italy [e]

P. G. Pelfer
University and INFN Florence, Florence, Italy [e]

A. Bamberger, D. Dobur, F. Karstens, N.N. Vlasov[18]
Fakultät für Physik der Universität Freiburg i.Br., Freiburg i.Br., Germany [b]

P.J. Bussey[19], A.T. Doyle, W. Dunne, M. Forrest, M. Rosin, D.H. Saxon, I.O. Skillicorn
Department of Physics and Astronomy, University of Glasgow, Glasgow, United Kingdom [m]

I. Gialas[20], K. Papageorgiu
Department of Engineering in Management and Finance, Univ. of Aegean, Greece

U. Holm, R. Klanner, E. Lohrmann, H. Perrey, P. Schleper, T. Schörner-Sadenius, J. Sztuk, H. Stadie, M. Turcato
Hamburg University, Institute of Exp. Physics, Hamburg, Germany [b]

C. Foudas, C. Fry, K.R. Long, A.D. Tapper
Imperial College London, High Energy Nuclear Physics Group, London, United Kingdom [m]

T. Matsumoto, K. Nagano, K. Tokushuku[21], S. Yamada, Y. Yamazaki[22]
Institute of Particle and Nuclear Studies, KEK, Tsukuba, Japan [f]

A.N. Barakbaev, E.G. Boos, N.S. Pokrovskiy, B.O. Zhautykov
Institute of Physics and Technology of Ministry of Education and Science of Kazakhstan, Almaty, Kazakhstan

V. Aushev[23], O. Bachynska, M. Borodin, I. Kadenko, A. Kozulia, V. Libov, D. Lontkovskyi, I. Makarenko, Iu. Sorokin, A. Verbytskyi, O. Volynets
Institute for Nuclear Research, National Academy of Sciences, Kiev and Kiev National University, Kiev, Ukraine

D. Son
Kyungpook National University, Center for High Energy Physics, Daegu, South Korea [g]

J. de Favereau, K. Piotrzkowski
Institut de Physique Nucléaire, Université Catholique de Louvain, Louvain-la-Neuve, Belgium [q]

F. Barreiro, C. Glasman, M. Jimenez, L. Labarga, J. del Peso, E. Ron, M. Soares, J. Terrón, C. Uribe-Estrada, M. Zambrana
Departamento de Física Teórica, Universidad Autónoma de Madrid, Madrid, Spain [l]

F. Corriveau, C. Liu, J. Schwartz, R. Walsh, C. Zhou
Department of Physics, McGill University, Montréal, Québec, Canada H3A 2T8 [a]

T. Tsurugai
Meiji Gakuin University, Faculty of General Education, Yokohama, Japan [f]

A. Antonov, B.A. Dolgoshein, D. Gladkov, V. Sosnovtsev, A. Stifutkin, S. Suchkov
Moscow Engineering Physics Institute, Moscow, Russia [j]

R.K. Dementiev, P.F. Ermolov †, L.K. Gladilin, Yu.A. Golubkov, L.A. Khein, I.A. Korzhavina, V.A. Kuzmin, B.B. Levchenko[24], O.Yu. Lukina, A.S. Proskuryakov, L.M. Shcheglova, D.S. Zotkin
Moscow State University, Institute of Nuclear Physics, Moscow, Russia [k]

I. Abt, A. Caldwell, D. Kollar, B. Reisert, W.B. Schmidke
Max-Planck-Institut für Physik, München, Germany

G. Grigorescu, A. Keramidas, E. Koffeman, P. Kooijman, A. Pellegrino, H. Tiecke, M. Vázquez[12], L. Wiggers
NIKHEF and University of Amsterdam, Amsterdam, Netherlands [h]

N. Brümmer, B. Bylsma, L.S. Durkin, A. Lee, T.Y. Ling
Physics Department, Ohio State University, Columbus, Ohio 43210 [n]

P.D. Allfrey, M.A. Bell, A.M. Cooper-Sarkar, R.C.E. Devenish, J. Ferrando, B. Foster, C. Gwenlan[25], K. Horton[26], K. Oliver, A. Robertson, R. Walczak
Department of Physics, University of Oxford, Oxford United Kingdom [m]

A. Bertolin, F. Dal Corso, S. Dusini, A. Longhin, L. Stanco
INFN Padova, Padova, Italy [e]

P. Bellan, R. Brugnera, R. Carlin, A. Garfagnini, S. Limentani
Dipartimento di Fisica dell' Università and INFN, Padova, Italy [e]

B.Y. Oh, A. Raval, J.J. Whitmore[27]
Department of Physics, Pennsylvania State University, University Park, Pennsylvania 16802 [o]

Y. Iga
Polytechnic University, Sagamihara, Japan [f]

G. D'Agostini, G. Marini, A. Nigro
Dipartimento di Fisica, Università 'La Sapienza' and INFN, Rome, Italy [e]

J.E. Cole[28], J.C. Hart
Rutherford Appleton Laboratory, Chilton, Didcot, Oxon, United Kingdom [m]

H. Abramowicz[29], R. Ingbir, S. Kananov, A. Levy, A. Stern
Raymond and Beverly Sackler Faculty of Exact Sciences, School of Physics, Tel Aviv University, Tel Aviv, Israel [d]

M. Kuze, J. Maeda
Department of Physics, Tokyo Institute of Technology, Tokyo, Japan [f]

R. Hori, S. Kagawa[30], N. Okazaki, S. Shimizu, T. Tawara
Department of Physics, University of Tokyo, Tokyo, Japan [f]

R. Hamatsu, H. Kaji[31], S. Kitamura[32], O. Ota[33], Y.D. Ri
Tokyo Metropolitan University, Department of Physics, Tokyo, Japan [f]

M. Costa, M.I. Ferrero, V. Monaco, R. Sacchi, V. Sola, A. Solano
Università di Torino and INFN, Torino, Italy [e]

M. Arneodo, M. Ruspa
Università del Piemonte Orientale, Novara, and INFN, Torino, Italy [e]

S. Fourletov[7], J.F. Martin, T.P. Stewart
Department of Physics, University of Toronto, Toronto, Ontario, Canada M5S 1A7 [a]

S.K. Boutle[20], J.M. Butterworth, T.W. Jones, J.H. Loizides, M. Wing[34]
Physics and Astronomy Department, University College London, London, United Kingdom [m]

B. Brzozowska, J. Ciborowski[35], G. Grzelak, P. Kulinski, P. Łużniak[36], J. Malka[36], R.J. Nowak, J.M. Pawlak, W. Perlanski[36], T. Tymieniecka[37], A.F. Żarnecki
Warsaw University, Institute of Experimental Physics, Warsaw, Poland

M. Adamus, P. Plucinski[38], A. Ukleja
Institute for Nuclear Studies, Warsaw, Poland

Y. Eisenberg, D. Hochman, U. Karshon
Department of Particle Physics, Weizmann Institute, Rehovot, Israel [c]

E. Brownson, D.D. Reeder, A.A. Savin, W.H. Smith, H. Wolfe
Department of Physics, University of Wisconsin, Madison, Wisconsin 53706, USA [n]

S. Bhadra, C.D. Catterall, Y. Cui, G. Hartner, S. Menary, U. Noor, J. Standage, J. Whyte
Department of Physics, York University, Ontario, Canada M3J 1P3 [a]

[1] also affiliated with University College London, United Kingdom
[2] now at University of Salerno, Italy
[3] also working at Max Planck Institute, Munich, Germany
[4] now at Institute of Aviation, Warsaw, Poland
[5] supported by the research grant no. 1 P03B 04529 (2005-2008)
[6] This work was supported in part by the Marie Curie Actions Transfer of Knowledge project COCOS (contract MTKD-CT-2004-517186)
[7] now at University of Bonn, Germany
[8] now at DESY group FEB, Hamburg, Germany
[9] also at Moscow State University, Russia
[10] now at University of Liverpool, UK
[11] on leave of absence at CERN, Geneva, Switzerland
[12] now at CERN, Geneva, Switzerland
[13] now at Bologna University, Bologna, Italy
[14] also at Institut of Theoretical and Experimental Physics, Moscow, Russia
[15] also at INP, Cracow, Poland
[16] also at FPACS, AGH-UST, Cracow, Poland
[17] partially supported by Warsaw University, Poland
[18] partly supported by Moscow State University, Russia
[19] Royal Society of Edinburgh, Scottish Executive Support Research Fellow
[20] also affiliated with DESY, Germany
[21] also at University of Tokyo, Japan
[22] now at Kobe University, Japan
[23] supported by DESY, Germany
[24] partly supported by Russian Foundation for Basic Research grant no. 05-02-39028-NSFC-a
[25] STFC Advanced Fellow
[26] nee Korcsak-Gorzo
[27] This material was based on work supported by the National Science Foundation, while working at the Foundation.
[28] now at University of Kansas, Lawrence, USA
[29] also at Max Planck Institute, Munich, Germany, Alexander von Humboldt Research Award
[30] now at KEK, Tsukuba, Japan
[31] now at Nagoya University, Japan
[32] member of Department of Radiological Science, Tokyo Metropolitan University, Japan
[33] now at SunMelx Co. Ltd., Tokyo, Japan
[34] also at Hamburg University, Inst. of Exp. Physics, Alexander von Humboldt Research Award and partially supported by DESY, Hamburg, Germany

[35] also at Łódź University, Poland
[36] member of Łódź University, Poland
[37] also at University of Podlasie, Siedlce, Poland
[38] now at Lund Universtiy, Lund, Sweden
[†] deceased

[a] supported by the Natural Sciences and Engineering Research Council of Canada (NSERC)

[b] supported by the German Federal Ministry for Education and Research (BMBF), under contract numbers 05 HZ6PDA, 05 HZ6GUA, 05 HZ6VFA and 05 HZ4KHA

[c] supported in part by the MINERVA Gesellschaft für Forschung GmbH, the Israel Science Foundation (grant no. 293/02-11.2) and the U.S.-Israel Binational Science Foundation

[d] supported by the Israel Science Foundation

[e] supported by the Italian National Institute for Nuclear Physics (INFN)

[f] supported by the Japanese Ministry of Education, Culture, Sports, Science and Technology (MEXT) and its grants for Scientific Research

[g] supported by the Korean Ministry of Education and Korea Science and Engineering Foundation

[h] supported by the Netherlands Foundation for Research on Matter (FOM)

[i] supported by the Polish State Committee for Scientific Research, project no. DESY/256/2006 - 154/DES/2006/03

[j] partially supported by the German Federal Ministry for Education and Research (BMBF)

[k] supported by RF Presidential grant N 1456.2008.2 for the leading scientific schools and by the Russian Ministry of Education and Science through its grant for Scientific Research on High Energy Physics

[l] supported by the Spanish Ministry of Education and Science through funds provided by CICYT

[m] supported by the Science and Technology Facilities Council, UK

[n] supported by the US Department of Energy

[o] supported by the US National Science Foundation. Any opinion, findings and conclusions or recommendations expressed in this material are those of the authors and do not necessarily reflect the views of the National Science Foundation.

[p] supported by the Polish Ministry of Science and Higher Education as a scientific project (2006-2008)

[q] supported by FNRS and its associated funds (IISN and FRIA) and by an Inter-University Attraction Poles Programme subsidised by the Belgian Federal Science Policy Office

[r] supported by an FRGS grant from the Malaysian government

1 Introduction

Jet production in ep collisions provides a wide testing ground of perturbative QCD (pQCD). Measurements of differential cross sections for jet production [1–3] have allowed detailed studies of parton dynamics, tests of the proton and photon parton distribution functions (PDFs) as well as precise determinations of the strong coupling constant, α_s.

Gluon emission from primary quarks was investigated [4, 5] by means of the internal structure of jets; these type of studies gave insight into the transition between a parton produced in a hard process and the experimentally observable jet of hadrons. The pattern of parton radiation within a jet is dictated in QCD by the splitting functions. These functions, $P_{ab}(z, \mu)$ with $a, b = q$ or g, are interpreted as the probability that a parton of type b, having radiated a parton of type a, is left with a fraction z of the longitudinal momentum of the parent parton and a transverse momentum squared smaller than μ^2, where μ is the typical hard scale of the process. The splitting functions are calculable as power series in α_s. Thus, the characteristics of jet substructure provide direct access to the QCD splitting functions and their dependence on the scale.

The understanding of jet substructure is also important in the context of jet identification in boosted systems, like hadronic top decays [6] or $b\bar{b}$ final states at LHC [7]. The first example calls for a direct application of jet substructure, the second requires knowledge about jet substructure to distinguish between single- and double-quark induced jets. This paper presents a study of jet substructure in a more controlled hadronic-type environment than that provided by hadron-hadron colliders.

Jet production in neutral current (NC) deep inelastic scattering (DIS) was previously used to study the mean subjet multiplicity [4] and the mean integrated jet shape [5] with values of $\alpha_s(M_Z)$ extracted from those measurements. In the present study, the pattern of QCD radiation is investigated by means of the subjet topology, providing a more stringent test of the pQCD calculations.

In this paper, measurements of normalised differential subjet cross sections for those jets which contain two subjets at a given resolution scale are presented. The measurements were done as functions of the ratio between the subjet transverse energy and that of the jet, $E_T^{\rm sbj}/E_T^{\rm jet}$, the difference between the subjet pseudorapidity[1] (azimuth) and that of the jet, $\eta^{\rm sbj} - \eta^{\rm jet}$ ($|\phi^{\rm sbj} - \phi^{\rm jet}|$), and $\alpha^{\rm sbj}$, the angle, as viewed from the jet centre, between the subjet with higher transverse energy and the proton beam line in the pseudorapidity-

[1] The ZEUS coordinate system is a right-handed Cartesian system, with the Z axis pointing in the proton beam direction, referred to as the "forward direction", and the X axis pointing left towards the centre of HERA. The coordinate origin is at the nominal interaction point. The pseudorapidity is defined as $\eta = -\ln(\tan\frac{\theta}{2})$, where the polar angle θ is taken with respect to the proton beam direction.

azimuth plane (see Fig. 1). The predictions of pQCD at next-to-leading order (NLO) were compared to the data.

2 Jets and subjets

The analysis of subjets presented in this paper was performed using the laboratory frame. In this frame, the calculations of the subjet distributions can be performed up to $\mathcal{O}(\alpha_s^2)$, i.e. NLO, with jets consisting of up to three partons. The analysis used events with high virtuality of the exchanged boson, Q^2; at low values of Q^2, the sample of events with at least one jet of high $E_T^{\rm jet}$ ($E_T^{\rm jet} \gg \sqrt{Q^2}$) is dominated by dijet events. In that case, the calculations include jets consisting of up to only two partons and, therefore, correspond to lowest-order predictions of jet substructure.

The k_T cluster algorithm [8] was used in the longitudinally invariant inclusive mode [9] to define jets in the hadronic final state. Subjets [10] were resolved within a jet by considering all particles associated with the jet and repeating the application of the k_T cluster algorithm until, for every pair of particles i and j the quantity $d_{ij} = \min(E_{T,i}, E_{T,j})^2 \cdot ((\eta_i - \eta_j)^2 + (\phi_i - \phi_j)^2)$, where $E_{T,i}$, η_i and ϕ_i are the transverse energy, pseudorapidity and azimuth of particle i, respectively, was greater than $d_{\rm cut} = y_{\rm cut} \cdot (E_T^{\rm jet})^2$. All remaining clusters were called subjets.

The subjet multiplicity depends upon the value chosen for the resolution parameter $y_{\rm cut}$. Subjet distributions were studied for those jets with exactly two subjets at a value of the resolution parameter of $y_{\rm cut} = 0.05$. This value of $y_{\rm cut}$ was chosen as a compromise between resolution, size of the hadronisation correction factors and statistics. The effect of the parton-to-hadron corrections on the shape of the subjet distributions becomes increasingly larger as $y_{\rm cut}$ decreases. On the other hand, the number of jets with exactly two subjets decreases rapidly as $y_{\rm cut}$ increases.

Subjet distributions were studied as functions of $E_T^{\rm sbj}/E_T^{\rm jet}$, $\eta^{\rm sbj} - \eta^{\rm jet}$, $|\phi^{\rm sbj} - \phi^{\rm jet}|$ and $\alpha^{\rm sbj}$. One of the goals of this study was to investigate the extent to which pQCD calculations are able to reproduce the observed distributions. In addition, the dependence of the splitting functions $P_{ab}(z, \mu)$ on z can be investigated using the $E_T^{\rm sbj}/E_T^{\rm jet}$ distribution. The splitting functions at leading order (LO) do not depend on μ but acquire a weak dependence due to higher-order corrections. Such a dependence can be investigated by measuring the subjet distributions in different regions of $E_T^{\rm jet}$ or Q^2.

The substructure of jets consisting of a quark-gluon pair (the quark-induced process $eq \to eqg$) or a quark-antiquark pair (the gluon-induced process $eg \to eq\bar{q}$) are predicted to be different (see Section 8.1). Furthermore, the relative contributions of quark- and gluon-induced processes vary with Bjorken x and Q^2. The predicted difference mentioned

above is amenable to experimental investigation by comparing the shape of the subjet distributions in different regions of x and Q^2.

Colour coherence leads to a suppression of soft-gluon radiation in certain regions of phase space. The effects of colour coherence between the initial and final states have been studied in hadron-hadron collisions [11]. These effects are also expected to appear in lepton-hadron collisions. For the process $eq \to eqg$, colour coherence implies a tendency of the subjet with lower (higher) transverse energy, $E_{T,\mathrm{low}}^{\mathrm{sbj}}$ ($E_{T,\mathrm{high}}^{\mathrm{sbj}}$), to have $\eta^{\mathrm{sbj}} - \eta^{\mathrm{jet}} > 0$ ($\eta^{\mathrm{sbj}} - \eta^{\mathrm{jet}} < 0$). The variable α^{sbj}, defined in close analogy to the variables used to study colour coherence in hadron-hadron collisions [11], reflects directly whether the subjet with the lower transverse energy has a tendency to be emitted towards the proton beam direction.

3 Experimental set-up

A detailed description of the ZEUS detector can be found elsewhere [12, 13]. A brief outline of the components most relevant for this analysis is given below.

Charged particles were tracked in the central tracking detector (CTD) [14], which operated in a magnetic field of 1.43 T provided by a thin superconducting solenoid. The CTD consisted of 72 cylindrical drift-chamber layers, organised in nine superlayers covering the polar-angle region $15^\circ < \theta < 164^\circ$. The transverse-momentum resolution for full-length tracks can be parameterised as $\sigma(p_T)/p_T = 0.0058 p_T \oplus 0.0065 \oplus 0.0014/p_T$, with p_T in GeV. The tracking system was used to measure the interaction vertex with a typical resolution along (transverse to) the beam direction of 0.4 (0.1) cm and to cross-check the energy scale of the calorimeter.

The high-resolution uranium–scintillator calorimeter (CAL) [15] covered 99.7% of the total solid angle and consisted of three parts: the forward (FCAL), the barrel (BCAL) and the rear (RCAL) calorimeters. Each part was subdivided transversely into towers and longitudinally into one electromagnetic section and either one (in RCAL) or two (in BCAL and FCAL) hadronic sections. The smallest subdivision of the calorimeter was called a cell. Under test-beam conditions, the CAL single-particle relative energy resolutions were $\sigma(E)/E = 0.18/\sqrt{E}$ for electrons and $\sigma(E)/E = 0.35/\sqrt{E}$ for hadrons, with E in GeV.

The luminosity was measured from the rate of the bremsstrahlung process $ep \to e\gamma p$. The resulting small-angle energetic photons were measured by the luminosity monitor [16], a lead–scintillator calorimeter placed in the HERA tunnel at $Z = -107$ m.

4 Data selection

The data were collected during the running period 1998–2000, when HERA operated with protons of energy $E_p = 920$ GeV and electrons or positrons[2] of energy $E_e = 27.5$ GeV, and correspond to an integrated luminosity of 81.7 ± 1.9 pb^{-1}.

Neutral current DIS events were selected offline using criteria similar to those reported previously [5]. The main steps are given below.

A reconstructed event vertex consistent with the nominal interaction position was required and cuts based on tracking information were applied to reduce the contamination from beam-induced and cosmic-ray background. The scattered-electron candidate was identified using the pattern of energy deposits in the CAL [17]. The energy, E'_e, and polar angle, θ_e, of the electron candidate were also determined from the CAL measurements. The double-angle method [18], which uses θ_e and an angle γ that corresponds, in the quark-parton model, to the direction of the scattered quark, was used to reconstruct Q^2. The angle γ was reconstructed using the CAL measurements of the hadronic final state.

Electron candidates were required to have an energy $E'_e > 10$ GeV, to ensure a high and well understood electron-finding efficiency and to suppress background from photoproduction. The inelasticity variable, y, as reconstructed using the electron energy and polar angle, was required to be below 0.95; this condition removed events in which fake electron candidates from photoproduction background were found in the FCAL. The requirement $38 < (E - p_Z) < 65$ GeV, where E is the total CAL energy and p_Z is the Z component of the energy measured in the CAL cells, was applied to remove events with large initial-state radiation and to reduce further the photoproduction background. Remaining cosmic rays and beam-related background were rejected by requiring the total missing transverse momentum, $p_T^{\rm miss}$, to be small compared to the total transverse energy, $E_T^{\rm tot}$, $p_T^{\rm miss}/\sqrt{E_T^{\rm tot}} < 3\ \sqrt{\rm GeV}$. The kinematic range was restricted to $Q^2 > 125$ GeV^2.

The k_T cluster algorithm was used in the longitudinally invariant inclusive mode to reconstruct jets in the measured hadronic final state from the energy deposits in the CAL cells. The jet algorithm was applied after excluding those cells associated with the scattered-electron candidate. Jet transverse-energy corrections were computed using the method developed in a previous analysis [5]. Events were required to have at least one jet of $E_T^{\rm jet} > 14$ GeV and $-1 < \eta^{\rm jet} < 2.5$. The final sample of 128986 events contained 132818 jets, of which 21162 jets had exactly two subjets at $y_{\rm cut} = 0.05$.

[2] In the following, the term "electron" denotes generically both the electron (e^-) and the positron (e^+).

5 Monte Carlo simulation

Samples of events were generated to determine the response of the detector to jets of hadrons and the correction factors necessary to obtain the hadron-level subjet cross sections. The hadron level is defined as those hadrons with lifetime $\tau \geq 10$ ps. The generated events were passed through the GEANT 3.13-based [19] ZEUS detector- and trigger-simulation programs [13]. They were reconstructed and analysed applying the same program chain as to the data.

Neutral current DIS events including radiative effects were simulated using the HERACLES 4.6.1 [20] program with the DJANGOH 1.1 [21] interface to the hadronisation programs. HERACLES includes corrections for initial- and final-state radiation, vertex and propagator terms, and two-boson exchange. The QCD cascade is simulated using the colour-dipole model (CDM) [22] including the LO QCD diagrams as implemented in ARIADNE 4.08 [23] and, alternatively, with the MEPS model of LEPTO 6.5 [24]. The CTEQ5D [25] proton PDFs were used for these simulations. Fragmentation into hadrons is performed using the Lund string model [26] as implemented in JETSET [27, 28].

The jet search was performed on the Monte Carlo (MC) events using the energy measured in the CAL cells in the same way as for the data. The same jet algorithm was also applied to the final-state particles (hadron level) and to the partons available after the parton shower (parton level) to compute hadronisation correction factors (see Section 6).

6 QCD calculations

The $\mathcal{O}(\alpha_s^2)$ NLO QCD calculations used to compare with the data are based on the program DISENT [29]. The calculations used a generalised version of the subtraction method [30] and were performed in the massless $\overline{\text{MS}}$ renormalisation and factorisation schemes. The number of flavours was set to five; the renormalisation (μ_R) and factorisation (μ_F) scales were set to $\mu_R = \mu_F = Q$; α_s was calculated at two loops using $\Lambda^{(5)}_{\overline{\text{MS}}} = 220$ MeV which corresponds to $\alpha_s(M_Z) = 0.118$. The ZEUS-S [31] parameterisations of the proton PDFs were used. The results obtained with DISENT were cross-checked by using the program NLOJET++ [32].

Since the measurements refer to jets of hadrons, whereas the QCD calculations refer to jets of partons, the predictions were corrected to the hadron level using the MC samples described in Section 5. The multiplicative correction factor, C_{had}, defined as the ratio of the cross section for subjets of hadrons to that of partons, was estimated with the LEPTO-MEPS model, since it reproduced the shape of the QCD calculations better.

The normalised cross-section calculations changed typically by less than $\pm 20\%$ upon application of the parton-to-hadron corrections, except at the edges of the distributions, where they changed by up to $\pm 50\%$. Other effects not accounted for in the calculations, namely QED radiative corrections and Z^0 exchange, were found to be very small for the normalised cross-section calculations and neglected.

The following theoretical uncertainties were considered (as examples of the size of the uncertainties, average values of the effect of each uncertainty on the normalised cross section as functions of $E_T^{\rm sbj}/E_T^{\rm jet}$, $\eta^{\rm sbj}-\eta^{\rm jet}$, $|\phi^{\rm sbj}-\phi^{\rm jet}|$ and $\alpha^{\rm sbj}$ are given in parentheses):

- the uncertainty in the modelling of the parton shower was estimated by using different models (see Section 5) to calculate the parton-to-hadron correction factors (5.6%, 13.2%, 7.6%, 5.3%);
- the uncertainty on the calculations due to higher-order terms was estimated by varying μ_R by a factor of two up and down (0.01%, 0.46%, 0.58%, 0.34%);
- the uncertainty on the calculations due to the choice of μ_F was estimated by varying μ_F by a factor of two up and down (0.05%, 0.43%, 0.11%, 0.12%);
- the uncertainty on the calculations due to those on the proton PDFs was estimated by repeating the calculations using 22 additional sets from the ZEUS analysis [31]; this analysis takes into account the statistical and correlated systematic experimental uncertainties of each data set used in the determination of the proton PDFs (0.07%, 0.18%, 0.12%, 0.05%);
- the uncertainty on the calculations due to that on $\alpha_s(M_Z)$ was estimated by repeating the calculations using two additional sets of proton PDFs, for which different values of $\alpha_s(M_Z)$ were assumed in the fits. The difference between the calculations using these various sets was scaled to reflect the uncertainty on the current world average of α_s [33] (0.02%, 0.04%, 0.05%, 0.01%).

These uncertainties were added in quadrature and are shown as hatched bands in the figures.

7 Corrections and systematic uncertainties

The sample of events generated with CDM, after applying the same offline selection as for the data, gives a reasonably good description of the measured distributions of the kinematic, jet and subjet variables; the description provided by the MEPS sample is somewhat poorer. The comparison of the measured subjet distributions and the MC simulations is shown in Fig. 2.

The normalised differential cross sections were obtained from the data using the bin-by-bin correction method,

$$\frac{1}{\sigma}\frac{d\sigma_i}{dA} = \frac{1}{\sigma}\frac{N_{\mathrm{data},i}}{\mathcal{L}\cdot\Delta A_i}\cdot\frac{N^{\mathrm{had}}_{\mathrm{MC},i}}{N^{\mathrm{det}}_{\mathrm{MC},i}},$$

where $N_{\mathrm{data},i}$ is the number of subjets in data in bin i of the subjet variable A, $N^{\mathrm{had}}_{\mathrm{MC},i}$ ($N^{\mathrm{det}}_{\mathrm{MC},i}$) is the number of subjets in MC at hadron (detector) level, $\mathcal{L}$ is the integrated luminosity and ΔA_i is the bin width. The MC samples of CDM and MEPS were used to compute the acceptance correction factors to the subjet distributions. These correction factors took into account the efficiency of the trigger, the selection criteria and the purity and efficiency of the jet and subjet reconstruction.

The following sources of systematic uncertainty were considered for the measured subjet cross sections (as examples of the size of the uncertainties, average values of the effect of each uncertainty on the normalised cross section as functions of $E_T^{\mathrm{sbj}}/E_T^{\mathrm{jet}}$, $\eta^{\mathrm{sbj}}-\eta^{\mathrm{jet}}$, $|\phi^{\mathrm{sbj}}-\phi^{\mathrm{jet}}|$ and α^{sbj} are given in parentheses):

- the deviations in the results obtained by using either CDM or MEPS to correct the data from their average were taken to represent systematic uncertainties due to the modelling of the parton shower (0.5%, 2.9%, 2.6%, 1.3%);
- variations in the simulation of the CAL response to low-energy particles (0.3%, 1.6%, 1.2%, 0.6%).

Other uncertainties, such as those arising from the uncertainty in the absolute energy scale of the jets [1, 34], the uncertainty in the simulation of the trigger and the uncertainty in the absolute energy scale of the electron candidate [35], were investigated and found to be negligible. The systematic uncertainties were added in quadrature to the statistical uncertainties and are shown as error bars in the figures.

8 Results

Normalised differential subjet cross sections were measured for $Q^2 > 125$ GeV^2 for jets with $E_T^{\mathrm{jet}} > 14$ GeV and $-1 < \eta^{\mathrm{jet}} < 2.5$ which have exactly two subjets for $y_{\mathrm{cut}} = 0.05$.

The distribution of the fraction of transverse energy, $(1/\sigma)(d\sigma/d(E_T^{\mathrm{sbj}}/E_T^{\mathrm{jet}}))$, is presented in Fig. 3a. It contains two entries per jet and is symmetric with respect to $E_T^{\mathrm{sbj}}/E_T^{\mathrm{jet}} = 0.5$ by construction. This distribution has a peak for $0.4 < E_T^{\mathrm{sbj}}/E_T^{\mathrm{jet}} < 0.6$, which shows that the two subjets tend to have similar transverse energies.

The $\eta^{\rm sbj} - \eta^{\rm jet}$ data distribution is shown in Fig. 3b and also has two entries per jet. The measured cross section has a two-peak structure; the dip around $\eta^{\rm sbj} - \eta^{\rm jet} = 0$ is due to the fact that the two subjets are not resolved when they are too close together.

Figure 3c presents the measured normalised cross section as a function of $|\phi^{\rm sbj} - \phi^{\rm jet}|$. There are two entries per jet in this distribution. The distribution has a peak for $0.2 < |\phi^{\rm sbj} - \phi^{\rm jet}| < 0.3$; the suppression around $|\phi^{\rm sbj} - \phi^{\rm jet}| = 0$ also arises from the fact that the two subjets are not resolved when they are too close together.

The data distribution as a function of $\alpha^{\rm sbj}$ (one entry per jet) increases as $\alpha^{\rm sbj}$ increases (see Fig. 3d). This shows that the subjet with higher transverse energy tends to be in the rear direction. This is consistent with the asymmetric peaks observed in the $\eta^{\rm sbj} - \eta^{\rm jet}$ distribution (see Fig. 3b). Figure 4 shows the $\eta^{\rm sbj} - \eta^{\rm jet}$ distribution for those jets which have two subjets with asymmetric $E_T^{\rm sbj}$ ($E_{T,\rm low}^{\rm sbj}/E_T^{\rm jet} < 0.4$, or, equivalently, $E_{T,\rm high}^{\rm sbj}/E_T^{\rm jet} > 0.6$), separately for the subjet with higher and lower $E_T^{\rm sbj}$. It is to be noted that since the jet axis is reconstructed as the transverse-energy-weighted average of the subjet axes, the subjet with higher $E_T^{\rm sbj}$ is constrained to be closer to the jet axis than that of the lower $E_T^{\rm sbj}$ subjet. The measured distributions show that the higher (lower) $E_T^{\rm sbj}$ subjet tends to be in the rear (forward) direction. All these observations support the expectation of the presence of colour-coherence effects between the initial and final states and, in particular, the tendency of the subjet with lower $E_T^{\rm sbj}$ to be emitted predominantly towards the proton beam direction.

8.1 Comparison with NLO QCD calculations

Next-to-leading-order QCD calculations are compared to the data in Figs. 3 and 4. The QCD predictions give an adequate description of the data. However, the data points are situated at the upper (lower) edge of the theoretical uncertainty in some regions of the subjet variables such as $E_T^{\rm sbj}/E_T^{\rm jet} \sim 0.5$, $|\phi^{\rm sbj} - \phi^{\rm jet}| \sim 0$, $\alpha^{\rm sbj} \sim 0$ and the peaks in the $\eta^{\rm sbj} - \eta^{\rm jet}$ distribution ($E_T^{\rm sbj}/E_T^{\rm jet} \sim 0.25$, $|\phi^{\rm sbj} - \phi^{\rm jet}| > 0.3$ and $|\eta^{\rm sbj} - \eta^{\rm jet}| > 0.5$). Since the calculations are normalised to unity, the uncertainties are correlated among the points; this correlation gives rise to the pulsating pattern exhibited by the theoretical uncertainties.

The calculation of the cross section as a function of $E_T^{\rm sbj}/E_T^{\rm jet}$ exhibits a peak at $0.4 < E_T^{\rm sbj}/E_T^{\rm jet} < 0.6$, as seen in the data. The calculations for the $\eta^{\rm sbj} - \eta^{\rm jet}$ and $\alpha^{\rm sbj}$ distributions predict that the subjet with higher transverse energy tends to be in the rear direction, in agreement with the data. This shows that the mechanism driving the subjet topology in the data is the $eq \to eqg$ and $eg \to eq\bar{q}$ subprocesses as implemented in the pQCD calculations.

To gain further insight into the pattern of parton radiation, the predictions for quark- and gluon-induced processes (see Section 2) are compared separately with the data in Fig. 5. The NLO calculations predict that the two-subjet rate is dominated by quark-induced processes: the relative contribution of quark- (gluon-) induced processes is 81% (19%). The shape of the predictions for these two types of processes are different; in quark-induced processes, the two subjets have more similar transverse energies (see Fig. 5a) and are closer to each other (see Fig. 5b and 5c) than in gluon-induced processes. The comparison with the measurements shows that the data are better described by the calculations for jets arising from a qg pair than those coming from a $q\bar{q}$ pair.

8.2 E_T^{jet}, Q^2 and x dependence of the subjet distributions

Figures 6 to 9 show the normalised differential subjet cross sections in different regions of E_T^{jet}. Even though the mean subjet multiplicity decreases with increasing E_T^{jet} [4], the measured normalised differential subjet cross sections have very similar shapes in all E_T^{jet} regions for all the observables considered. This means that the subjet topology does not change significantly with E_T^{jet}. This is better illustrated in Fig. 10, where the data for all E_T^{jet} regions are plotted together. In particular, it is observed that the maximum of each measured normalised cross section in every region of E_T^{jet} occurs in the same bin of the distribution. To quantify the E_T^{jet} dependence more precisely, Fig. 11 shows the maximum value of the measured normalised cross section for each observable as a function of E_T^{jet} together with the NLO predictions. The spread of the measured maximum values of the normalised cross sections is $\pm(4-6)\%$. For each observable, the scaling behaviour of the normalised differential subjet cross sections is clearly observed and in agreement with the expectation that the splitting functions depend weakly on the energy scale. The NLO QCD calculations are in agreement with the data and support this observation.

Figures 12 to 15 show the normalised differential subjet cross sections in different regions of Q^2. In this case, it is observed that while the shape of the $E_T^{\mathrm{sbj}}/E_T^{\mathrm{jet}}$ distribution does not change significantly with Q^2, some dependence can be seen in the other observables. For example, the dip in the $\eta^{\mathrm{sbj}}-\eta^{\mathrm{jet}}$ distribution is shallower for $125 < Q^2 < 250$ GeV^2 than at higher Q^2 and the shape of the α^{sbj} distribution for $125 < Q^2 < 250$ GeV^2 is somewhat different than for the other regions (see Fig. 16). These features of the data are reasonably reproduced by the NLO QCD calculations and understood as a combination of two effects: the fraction of gluon-induced events is predicted to be 32% for $125 < Q^2 < 250$ GeV^2 and below 14% for higher Q^2; the shape of the normalised cross sections as functions of $\eta^{\mathrm{sbj}}-\eta^{\mathrm{jet}}$ and α^{sbj} changes from the region $125 < Q^2 < 250$ GeV^2 to $250 < Q^2 < 500$ GeV^2 (see Fig. 17) for quark- and gluon-induced events. It is observed that the maximum of each measured normalised cross section in every region of Q^2 occurs in the same bin

of the distribution, except for $|\phi^{\rm sbj} - \phi^{\rm jet}|$ in the highest-Q^2 region. Figure 18 shows the maximum[3] value of the measured normalised cross section for each observable as a function of Q^2 together with the NLO predictions. The spread of the measured maximum values of the normalised cross sections as functions of $E_T^{\rm sbj}/E_T^{\rm jet}$ and $|\phi^{\rm sbj} - \phi^{\rm jet}|$ is $\pm(3-4)\%$. On the other hand, the measured and predicted maximum values for the normalised cross sections as functions of $\eta^{\rm sbj} - \eta^{\rm jet}$ and $\alpha^{\rm sbj}$ exhibit a step-like behaviour between the lowest-Q^2 region and the rest.

Figures 19 to 22 show the normalised differential subjet cross sections in different regions of x. Figure 23 shows the data for all x regions plotted together. It is observed that the maximum of each measured normalised cross section in every region of x occurs in the same bin of the distribution, except for $|\phi^{\rm sbj} - \phi^{\rm jet}|$ in the highest x region. Figure 24 shows the maximum[3] value of the measured normalised cross section for each observable as a function of x. The shape of the $E_T^{\rm sbj}/E_T^{\rm jet}$ measured distribution does not change significantly with x, whereas some dependence is expected (see Fig. 24a). The dependence of the $\eta^{\rm sbj} - \eta^{\rm jet}$ and $\alpha^{\rm sbj}$ distributions with x exhibits features similar to those observed in the study of the Q^2 dependence; in particular, the maximum values (see Figs. 24b and 24d) exhibit a monotonic increase as x increases, which is reasonably reproduced by the calculations. As discussed previously, these features are understood as a combination of two effects: a decrease of the predicted fraction of gluon-induced events from 44% for $0.004 < x < 0.009$ to 6% for $x > 0.093$ and the change in shape of the normalised cross sections for quark- and gluon-induced processes as x increases (see Fig. 25).

To investigate the origin of the change in shape of the normalised differential cross sections between the lowest and higher Q^2 and x regions, LO and NLO calculations were compared. The most dramatic change is observed when restricting the kinematic region to $125 < Q^2 < 250$ GeV^2 or $0.004 < x < 0.009$ (see Fig. 26); the LO calculation of the $\eta^{\rm sbj} - \eta^{\rm jet}$ distribution does not exhibit a two-peak structure as seen in the NLO prediction and in the data. In addition, the LO calculation of the $\alpha^{\rm sbj}$ distribution peaks at $\alpha^{\rm sbj} \sim \pi/2$ in contrast with the NLO prediction and the data. This proves that the NLO QCD radiative corrections are responsible for these variations in shape and necessary for describing the data.

In summary, while the shapes of the normalised differential cross sections show only a weak dependence on $E_T^{\rm jet}$, their dependence on Q^2 and x have some prominent features at low Q^2 or x. The weak dependence on $E_T^{\rm jet}$ is consistent with the expected scaling behaviour of the splitting functions; however, the restriction to low Q^2 or x values demonstrates that the NLO QCD radiative corrections are important there. The NLO QCD calculations, which include the two competing processes $eq \to eqg$ and $eg \to eq\bar{q}$ and radiative corrections,

[3] For the $|\phi^{\rm sbj} - \phi^{\rm jet}|$ distribution, the same bin has been used for consistency.

adequately reproduce the measurements.

9 Summary

Normalised differential subjet cross sections in inclusive-jet NC DIS were measured in ep collisions using 81.7 pb^{-1} of data collected with the ZEUS detector at HERA. The cross sections refer to jets identified in the laboratory frame with the k_T cluster algorithm in the longitudinally invariant inclusive mode and selected with $E_T^{\rm jet} > 14$ GeV and $-1 < \eta^{\rm jet} < 2.5$. The measurements were made for those jets which have exactly two subjets for $y_{\rm cut} = 0.05$ in the kinematic region defined by $Q^2 > 125$ GeV^2.

The cross sections were measured as functions of $E_T^{\rm sbj}/E_T^{\rm jet}$, $\eta^{\rm sbj} - \eta^{\rm jet}$, $|\phi^{\rm sbj} - \phi^{\rm jet}|$ and $\alpha^{\rm sbj}$. The data show that the two subjets tend to have similar transverse energies and that the subjet with higher transverse energy tends to be in the rear direction. This is consistent with the effects of colour coherence between the initial and final states, which predict that soft parton radiation is emitted predominantly towards the proton beam direction.

An adequate description of the data is given by NLO QCD calculations. This means that the pattern of parton radiation as predicted by QCD reproduces the subjet topology in the data. Furthermore, the subjet distributions in the data are better described by the calculations for jets arising from a quark-gluon pair.

The normalised cross sections show a weak dependence on $E_T^{\rm jet}$, in agreement with the expected scaling behaviour of the splitting functions. By restricting the measurements to low Q^2 or x values, significant differences in shape are observed, which can be primarily attributed to NLO QCD radiative corrections.

Acknowledgements

We thank the DESY Directorate for their strong support and encouragement. We appreciate the contributions to the construction and maintenance of the ZEUS detector of many people who are not listed as authors. The HERA machine group and the DESY computing staff are especially acknowledged for their success in providing excellent operation of the collider and the data-analysis environment.

References

[1] ZEUS Coll., S. Chekanov et al., Phys. Lett. B 531 (2002) 9;
ZEUS Coll., S. Chekanov et al., Eur. Phys. J. C 23 (2002) 615.

[2] ZEUS Coll., J. Breitweg et al., Phys. Lett. B 443 (1998) 394;
ZEUS Coll., J. Breitweg et al., Phys. Lett. B 507 (2001) 70;
ZEUS Coll., S. Chekanov et al., Phys. Lett. B 547 (2002) 164;
ZEUS Coll., S. Chekanov et al., Eur. Phys. J. C 23 (2002) 13;
ZEUS Coll., S. Chekanov et al., Phys. Lett. B 560 (2003) 7;
ZEUS Coll., S. Chekanov et al., Eur. Phys. J. C 31 (2003) 149;
ZEUS Coll., S. Chekanov et al., Nucl. Phys. B 765 (2007) 1;
ZEUS Coll., S. Chekanov et al., Phys. Lett. B 649 (2007) 12.

[3] H1 Coll., C. Adloff et al., Phys. Lett. B 515 (2001) 17;
H1 Coll., C. Adloff et al., Eur. Phys. J. C 19 (2001) 289;
H1 Coll., C. Adloff et al., Eur. Phys. J. C 19 (2001) 429;
H1 Coll., C. Adloff et al., Eur. Phys. J. C 25 (2002) 13;
H1 Coll., C. Adloff et al., Phys. Lett. B 542 (2002) 193;
H1 Coll., C. Adloff et al., Eur. Phys. J. C 29 (2003) 497;
H1 Coll., A. Aktas et al., Phys. Lett. B 639 (2006) 21;
H1 Coll., A. Aktas et al., Phys. Lett. B 653 (2007) 134.

[4] ZEUS Coll., S. Chekanov et al., Phys. Lett. B 558 (2003) 41.

[5] ZEUS Coll., S. Chekanov et al., Nucl. Phys. B 700 (2004) 3.

[6] J. Thaler and L.-T. Wang, JHEP 0807 (2008) 092;
D.E. Kaplan et al., Preprint hep-ph/0806.0848, 2008.

[7] J.M. Butterworth et al., Phys. Rev. Lett. 100 (2008) 242001.

[8] S. Catani et al., Nucl. Phys. B 406 (1993) 187.

[9] S.D. Ellis and D.E. Soper, Phys. Rev. D 48 (1993) 3160.

[10] S. Catani et al., Nucl. Phys. B 383 (1992) 419;
M.H. Seymour, Nucl. Phys. B 421 (1994) 545;
M.H. Seymour, Phys. Lett. B 378 (1996) 279;
J.R. Forshaw and M.H. Seymour, JHEP 9909 (1999) 009.

[11] CDF Coll., F. Abe et al., Phys. Rev. D 50 (1994) 5562.

[12] ZEUS Coll., M. Derrick et al., Phys. Lett. B 293 (1992) 465.

[13] ZEUS Coll., U. Holm (ed.), *The ZEUS Detector*. Status Report (unpublished), DESY (1993), available on `http://www-zeus.desy.de/bluebook/bluebook.html`.

[14] N. Harnew et al., Nucl. Instr. Meth. A 279 (1989) 290;
B. Foster et al., Nucl. Phys. Proc. Suppl. B 32 (1993) 181;
B. Foster et al., Nucl. Instr. Meth. A 338 (1994) 254.

[15] M. Derrick et al., Nucl. Instr. Meth. A 309 (1991) 77;
A. Andresen et al., Nucl. Instr. Meth. A 309 (1991) 101;
A. Caldwell et al., Nucl. Instr. Meth. A 321 (1992) 356;
A. Bernstein et al., Nucl. Instr. Meth. A 336 (1993) 23.

[16] J. Andruszków et al., Preprint DESY-92-066, DESY, 1992;
ZEUS Coll., M. Derrick et al., Z. Phys. C 63 (1994) 391;
J. Andruszków et al., Acta Phys. Pol. B 32 (2001) 2025.

[17] H. Abramowicz, A. Caldwell and R. Sinkus, Nucl. Instr. Meth. A 365 (1995) 508;
R. Sinkus and T. Voss, Nucl. Instr. Meth. A 391 (1997) 360.

[18] S. Bentvelsen, J. Engelen and P. Kooijman, *Proc. of the Workshop on Physics at HERA*, W. Buchmüller and G. Ingelman (eds.), Vol. 1, p. 23. Hamburg, Germany, DESY (1992);
K.C. Höger, ibid., p. 43.

[19] R. Brun et al., GEANT3, Technical Report CERN-DD/EE/84-1, CERN, 1987.

[20] A. Kwiatkowski, H. Spiesberger and H.-J. Möhring, Comput. Phys. Comm. 69 (1992) 155;
H. Spiesberger, *An Event Generator for ep Interactions at HERA Including Radiative Processes (Version 4.6)*, 1996, available on `http://www.desy.de/~hspiesb/heracles.html`.

[21] K. Charchuła, G.A. Schuler and H. Spiesberger, Comput. Phys. Comm. 81 (1994) 381;
H. Spiesberger, HERACLES *and* DJANGOH*: Event Generation for ep Interactions at HERA Including Radiative Processes*, 1998, available on `http://wwwthep.physik.uni-mainz.de/~hspiesb/djangoh/djangoh.html`.

[22] Y. Azimov et al., Phys. Lett. B 165 (1985) 147;
G. Gustafson, Phys. Lett. B 175 (1986) 453;
G. Gustafson and U. Pettersson, Nucl. Phys. B 306 (1988) 746;
B. Andersson et al., Z. Phys. C 43 (1989) 625.

[23] L. Lönnblad, Comput. Phys. Comm. 71 (1992) 15;
L. Lönnblad, Z. Phys. C 65 (1995) 285.

[24] G. Ingelman, A. Edin and J. Rathsman, Comput. Phys. Comm. 101 (1997) 108.

[25] H.L. Lai et al., Eur. Phys. J. C 12 (2000) 375.

[26] B. Andersson et al., Phys. Rep. 97 (1983) 31.

[27] T. Sjöstrand, Comput. Phys. Comm. 82 (1994) 74;
T. Sjöstrand et al., Comput. Phys. Comm. 135 (2001) 238.

[28] T. Sjöstrand, Comput. Phys. Comm. 39 (1986) 347;
T. Sjöstrand and M. Bengtsson, Comput. Phys. Comm. 43 (1987) 367.

[29] S. Catani and M.H. Seymour, Nucl. Phys. B 485 (1997) 291. Erratum in Nucl. Phys. **B 510** (1998) 503.

[30] R.K. Ellis, D.A. Ross and A.E. Terrano, Nucl. Phys. B 178 (1981) 421.

[31] ZEUS Coll., S. Chekanov et al., Phys. Rev. D 67 (2003) 012007.

[32] Z. Nagy and Z. Trocsanyi, Phys. Rev. Lett. 87 (2001) 082001.

[33] S. Bethke, J. Phys. G 26 (2000) R27. Updated in S. Bethke, Prog. Part. Nucl. Phys. 58 (2007) 351.

[34] M. Wing (on behalf of the ZEUS Coll.), *Proc. of the 10th International Conference on Calorimetry in High Energy Physics*, R. Zhu (ed.), p. 767. Pasadena, USA (2002). Also in preprint hep-ex/0206036.

[35] ZEUS Coll., S. Chekanov et al., Eur. Phys. J. C 21 (2001) 443.

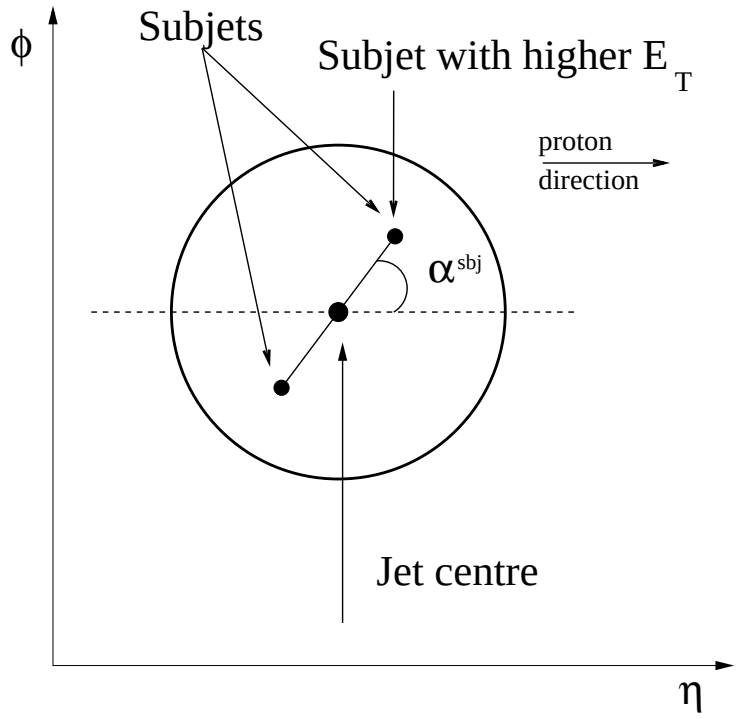

Figure 1: *Schematic representation of the α^{sbj} variable.*

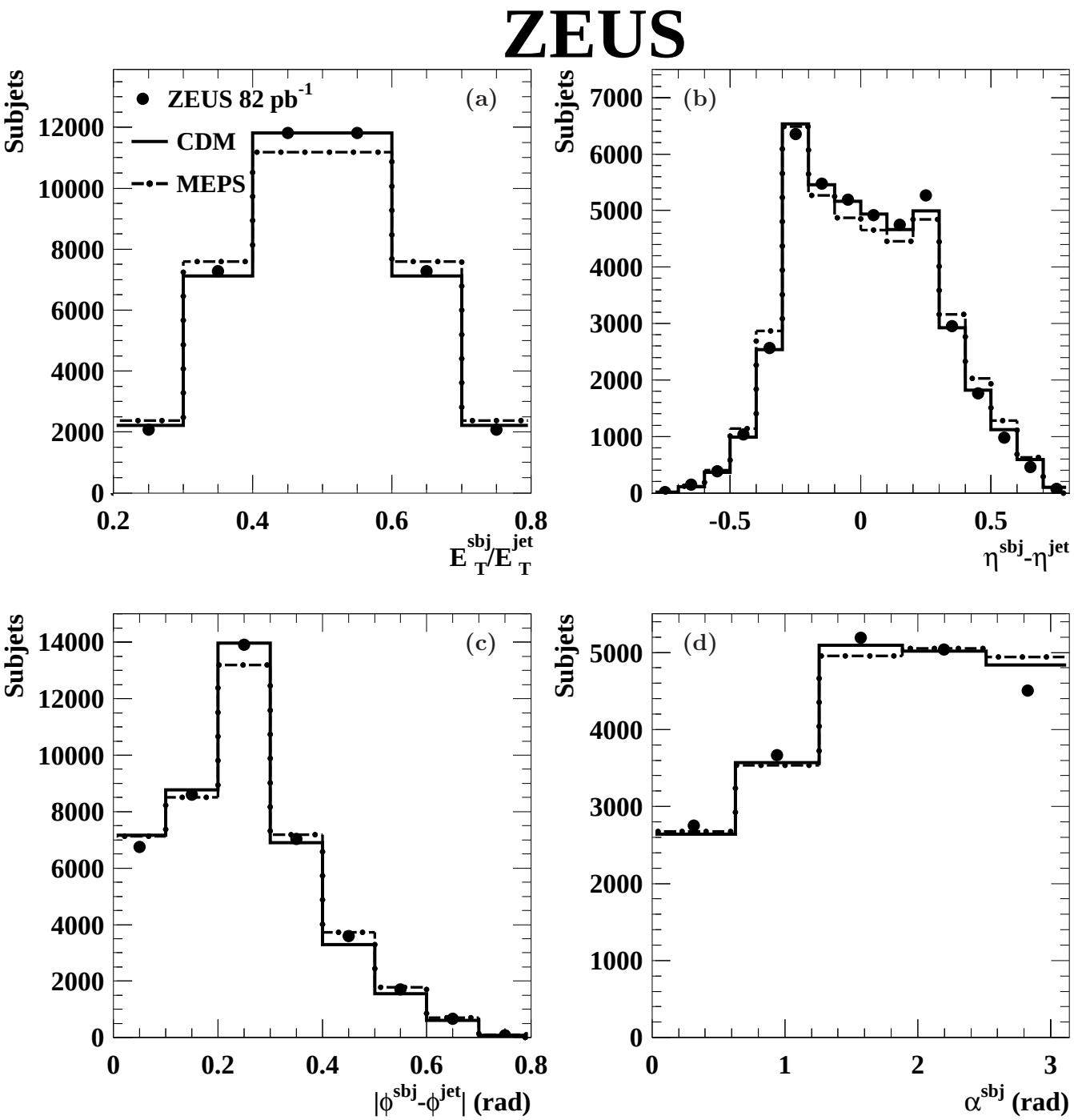

Figure 2: *Detector-level normalised subjet data distributions (dots) for jets with* $E_T^{\rm jet} > 14$ *GeV and* $-1 < \eta^{\rm jet} < 2.5$ *which have two subjets for* $y_{\rm cut} = 0.05$ *in the kinematic region given by* $Q^2 > 125$ *GeV*^{2} *as functions of (a)* $E_T^{\rm sbj}/E_T^{\rm jet}$*, (b)* $\eta^{\rm sbj} - \eta^{\rm jet}$*, (c)* $|\phi^{\rm sbj} - \phi^{\rm jet}|$ *and (d)* $\alpha^{\rm sbj}$*. The statistical uncertainties are smaller than the marker size. For comparison, the distributions of the CDM (solid histograms) and MEPS (dot-dashed histograms) Monte Carlo models are included.*

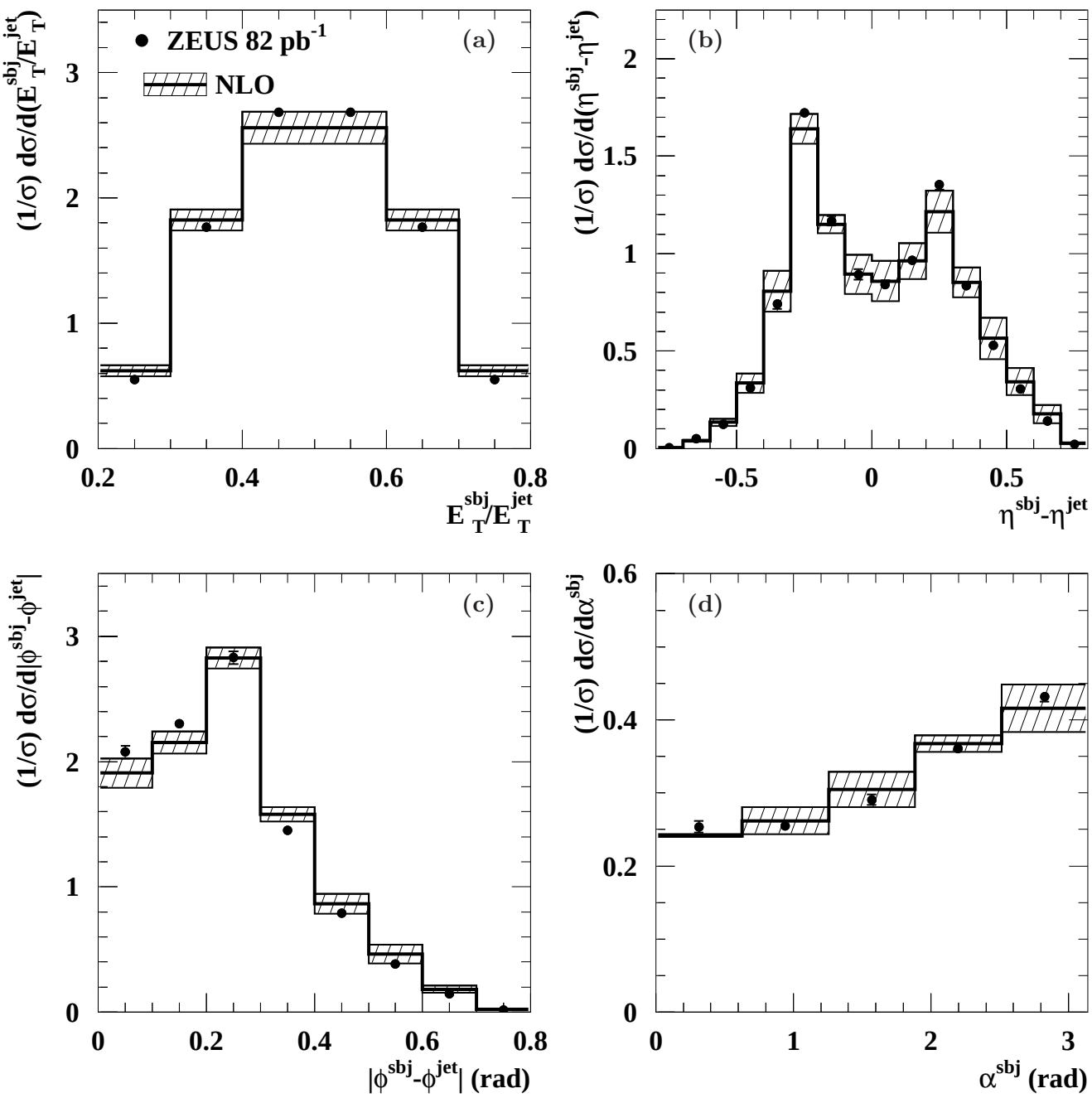

Figure 3: *Measured normalised differential subjet cross sections (dots) for jets with* $E_T^{\rm jet} > 14$ *GeV and* $-1 < \eta^{\rm jet} < 2.5$ *which have two subjets for* $y_{\rm cut} = 0.05$ *in the kinematic region given by* $Q^2 > 125$ *GeV*^{2} *as functions of (a)* $E_T^{\rm sbj}/E_T^{\rm jet}$*, (b)* $\eta^{\rm sbj} - \eta^{\rm jet}$*, (c)* $|\phi^{\rm sbj} - \phi^{\rm jet}|$ *and (d)* $\alpha^{\rm sbj}$*. The inner error bars represent the statistical uncertainties of the data, the outer error bars show the statistical and systematic uncertainties added in quadrature. In many cases, the error bars are smaller than the marker size and are therefore not visible. For comparison, the NLO QCD predictions (solid histograms) are included. The hatched bands represent the theoretical uncertainty.*

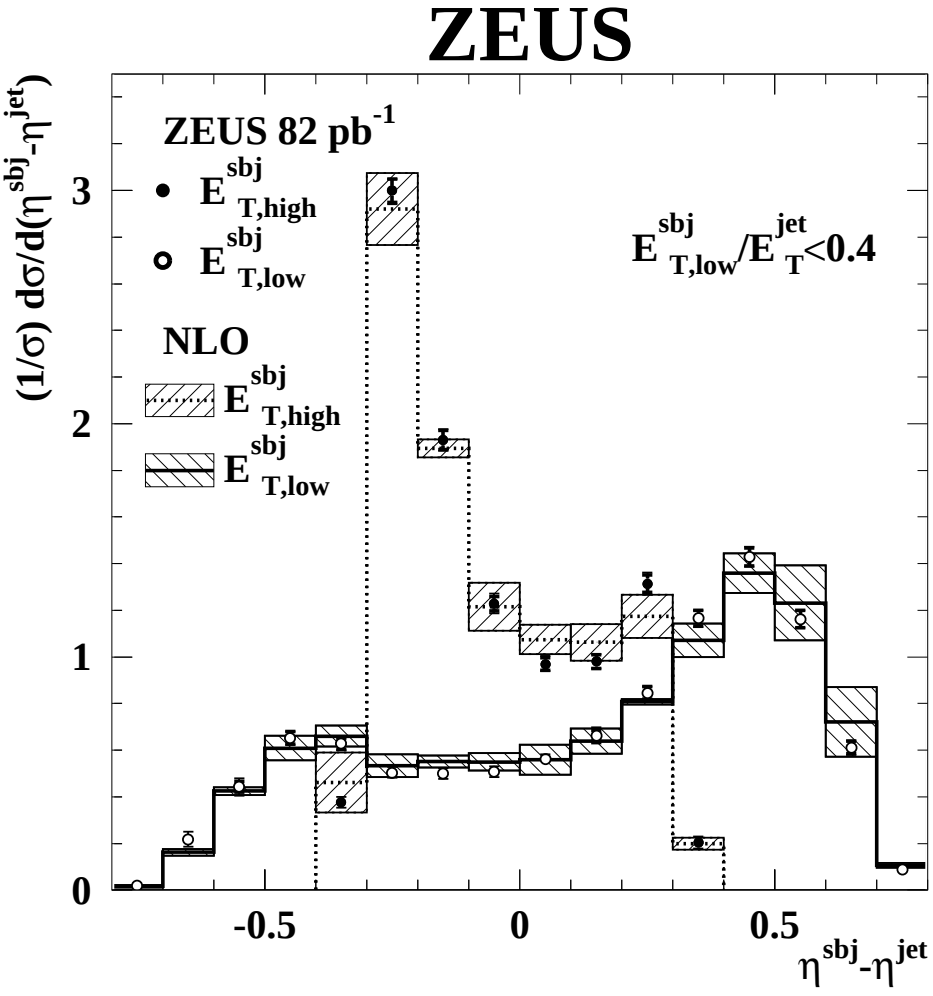

Figure 4: *Measured normalised differential subjet cross sections for jets with* $E_T^{\rm jet} > 14$ *GeV and* $-1 < \eta^{\rm jet} < 2.5$ *which have two subjets for* $y_{\rm cut} = 0.05$ *in the kinematic region given by* $Q^2 > 125$ *GeV*^{2} *and* $E_{T,\rm low}^{\rm sbj}/E_T^{\rm jet} < 0.4$ *as functions of* $\eta^{\rm sbj} - \eta^{\rm jet}$ *separately for the higher (dots) and lower (open circles)* $E_T^{\rm sbj}$ *subjets. Other details are as in the caption to Fig. 3.*

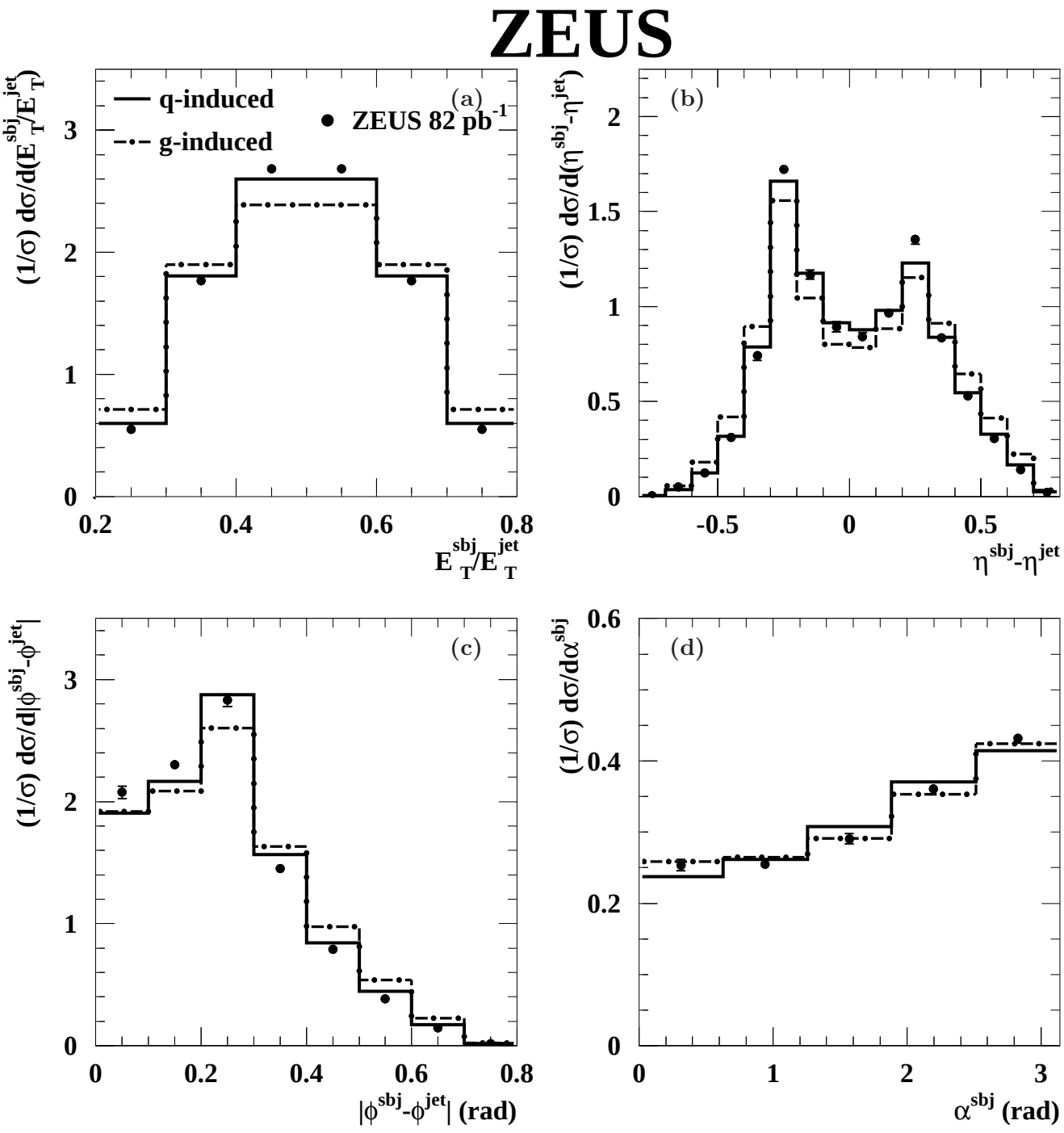

Figure 5: *Measured normalised differential subjet cross sections (dots) for jets with $E_T^{\rm jet} > 14$ GeV and $-1 < \eta^{\rm jet} < 2.5$ which have two subjets for $y_{\rm cut} = 0.05$ in the kinematic region given by $Q^2 > 125$ GeV^2 as functions of (a) $E_T^{\rm sbj}/E_T^{\rm jet}$, (b) $\eta^{\rm sbj} - \eta^{\rm jet}$, (c) $|\phi^{\rm sbj} - \phi^{\rm jet}|$ and (d) $\alpha^{\rm sbj}$. For comparison, the NLO predictions for quark- (solid histograms) and gluon-induced (dot-dashed histograms) processes are included. Other details are as in the caption to Fig. 3.*

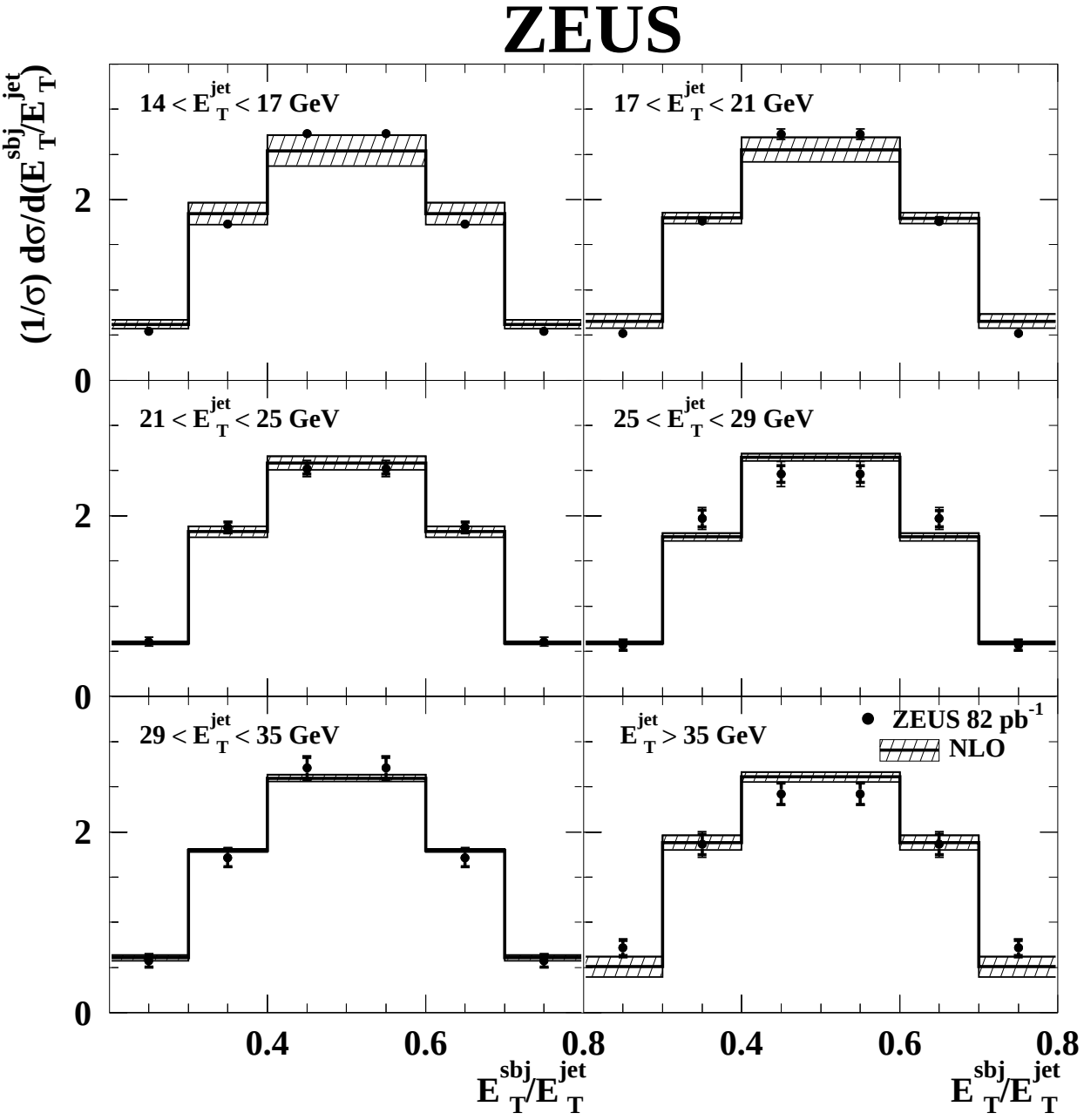

Figure 6: *Measured normalised differential subjet cross sections (dots) for jets with $E_T^{\rm jet} > 14$ GeV and $-1 < \eta^{\rm jet} < 2.5$ which have two subjets for $y_{\rm cut} = 0.05$ in the kinematic region given by $Q^2 > 125$ GeV^2 as functions of $E_T^{\rm sbj}/E_T^{\rm jet}$ in different regions of $E_T^{\rm jet}$. Other details are as in the caption to Fig. 3.*

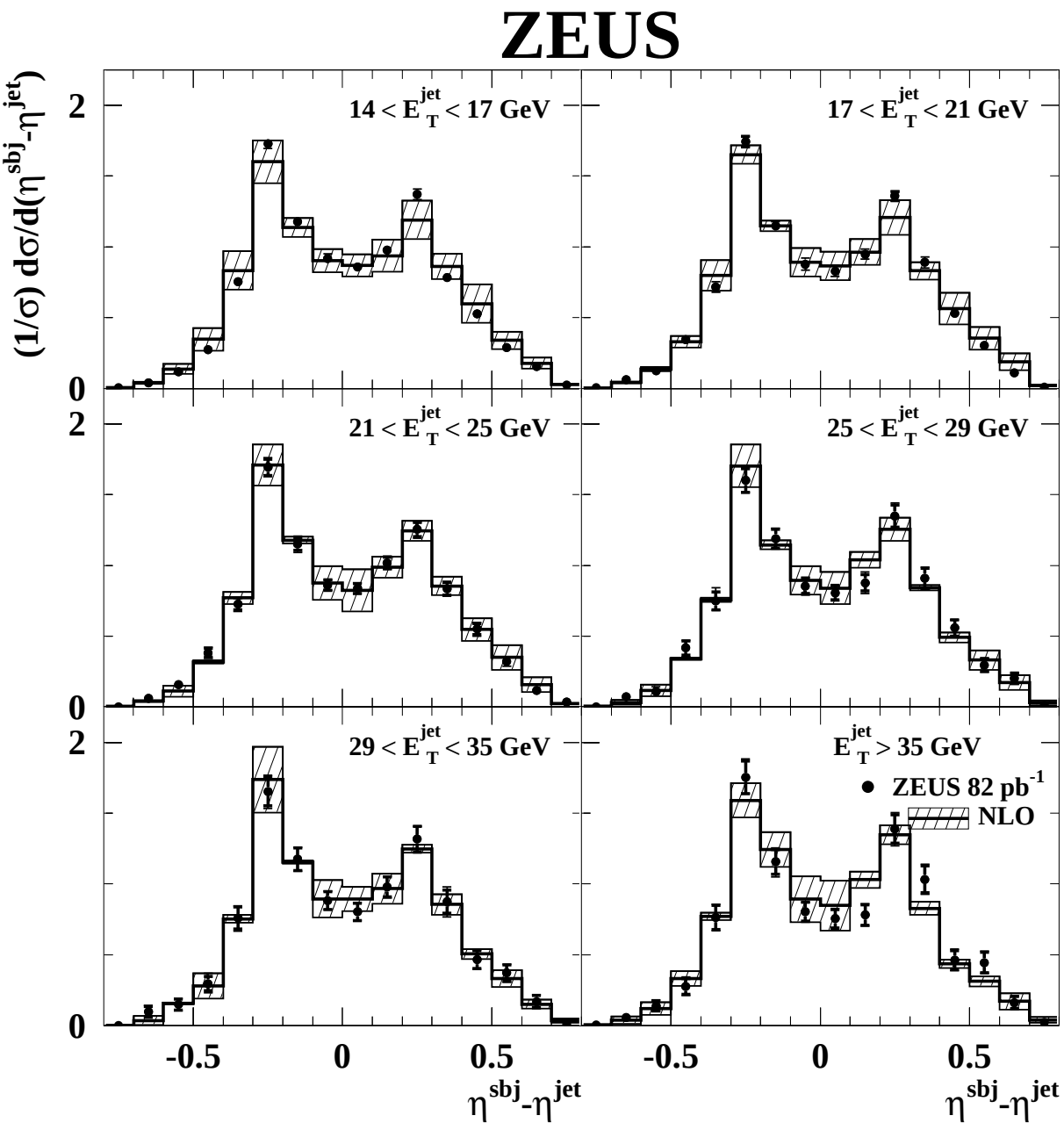

Figure 7: *Measured normalised differential subjet cross sections (dots) for jets with $E_T^{\rm jet} > 14$ GeV and $-1 < \eta^{\rm jet} < 2.5$ which have two subjets for $y_{\rm cut} = 0.05$ in the kinematic region given by $Q^2 > 125$ GeV^2 as functions of $\eta^{\rm sbj} - \eta^{\rm jet}$ in different regions of $E_T^{\rm jet}$. Other details are as in the caption to Fig. 3.*

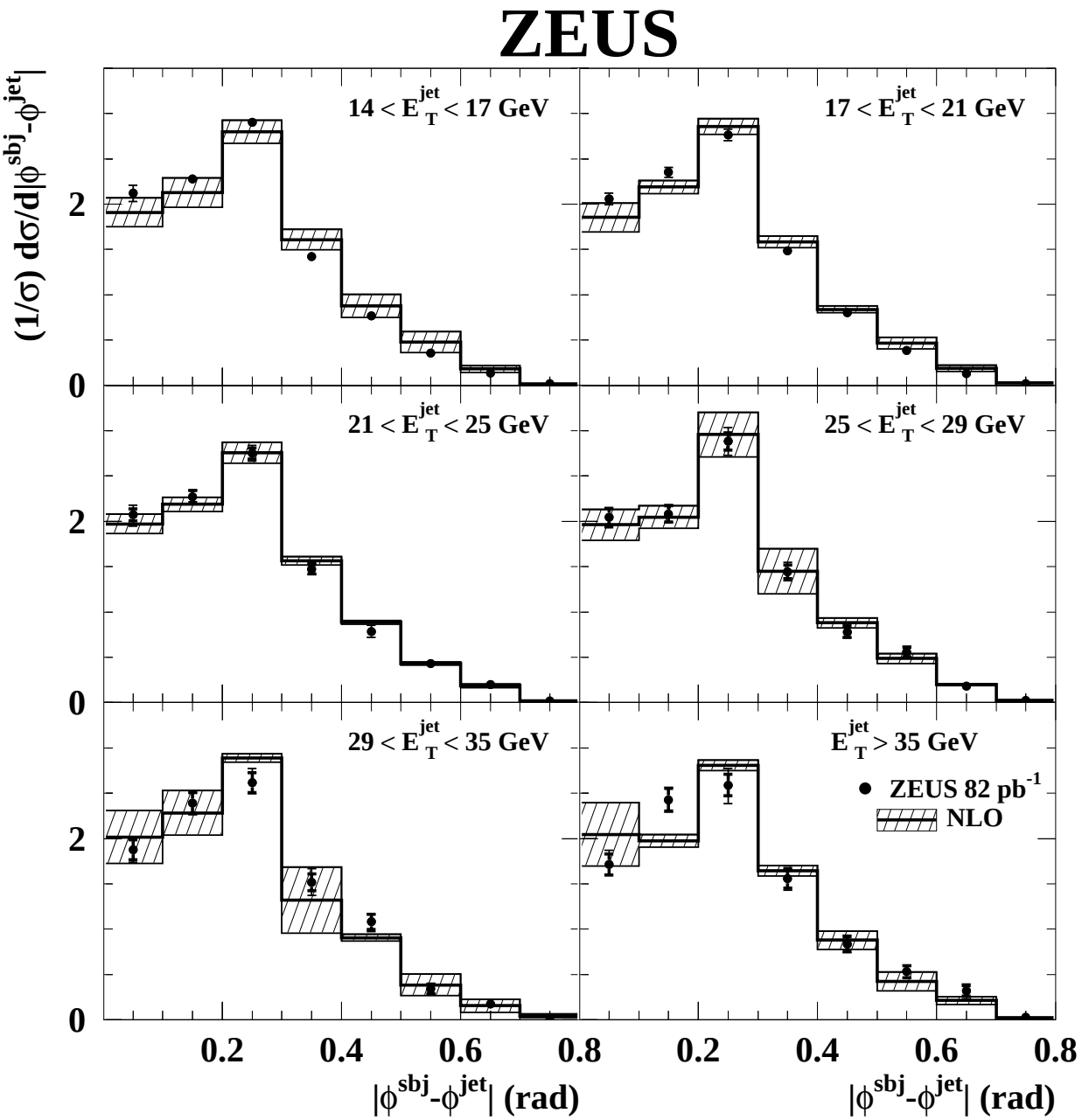

Figure 8: *Measured normalised differential subjet cross sections (dots) for jets with $E_T^{\rm jet} > 14$ GeV and $-1 < \eta^{\rm jet} < 2.5$ which have two subjets for $y_{\rm cut} = 0.05$ in the kinematic region given by $Q^2 > 125$ GeV^2 as functions of $|\phi^{\rm sbj} - \phi^{\rm jet}|$ in different regions of $E_T^{\rm jet}$. Other details are as in the caption to Fig. 3.*

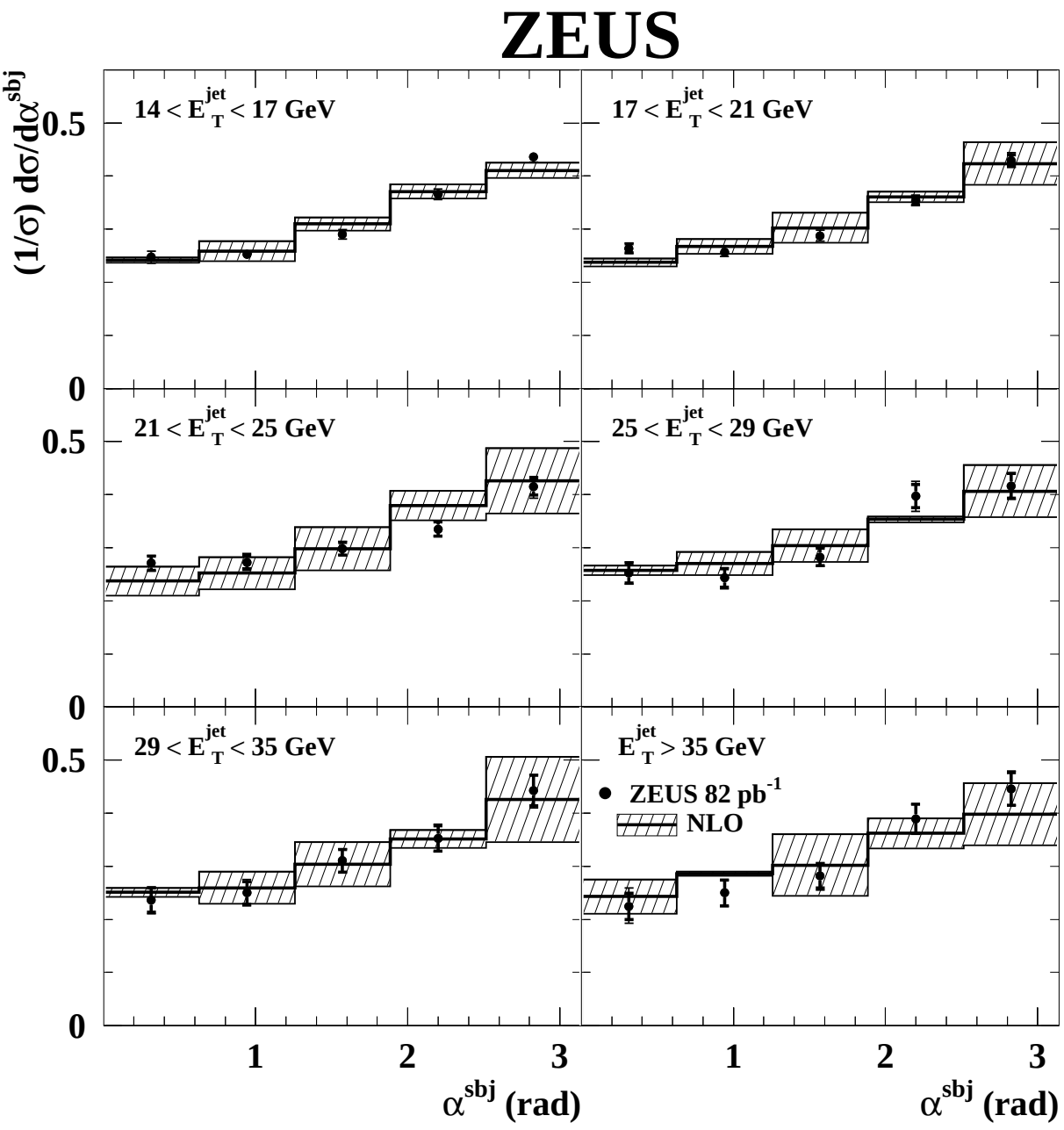

Figure 9: *Measured normalised differential subjet cross sections (dots) for jets with $E_T^{\rm jet} > 14$ GeV and $-1 < \eta^{\rm jet} < 2.5$ which have two subjets for $y_{\rm cut} = 0.05$ in the kinematic region given by $Q^2 > 125$ GeV^2 as functions of $\alpha^{\rm sbj}$ in different regions of $E_T^{\rm jet}$. Other details are as in the caption to Fig. 3.*

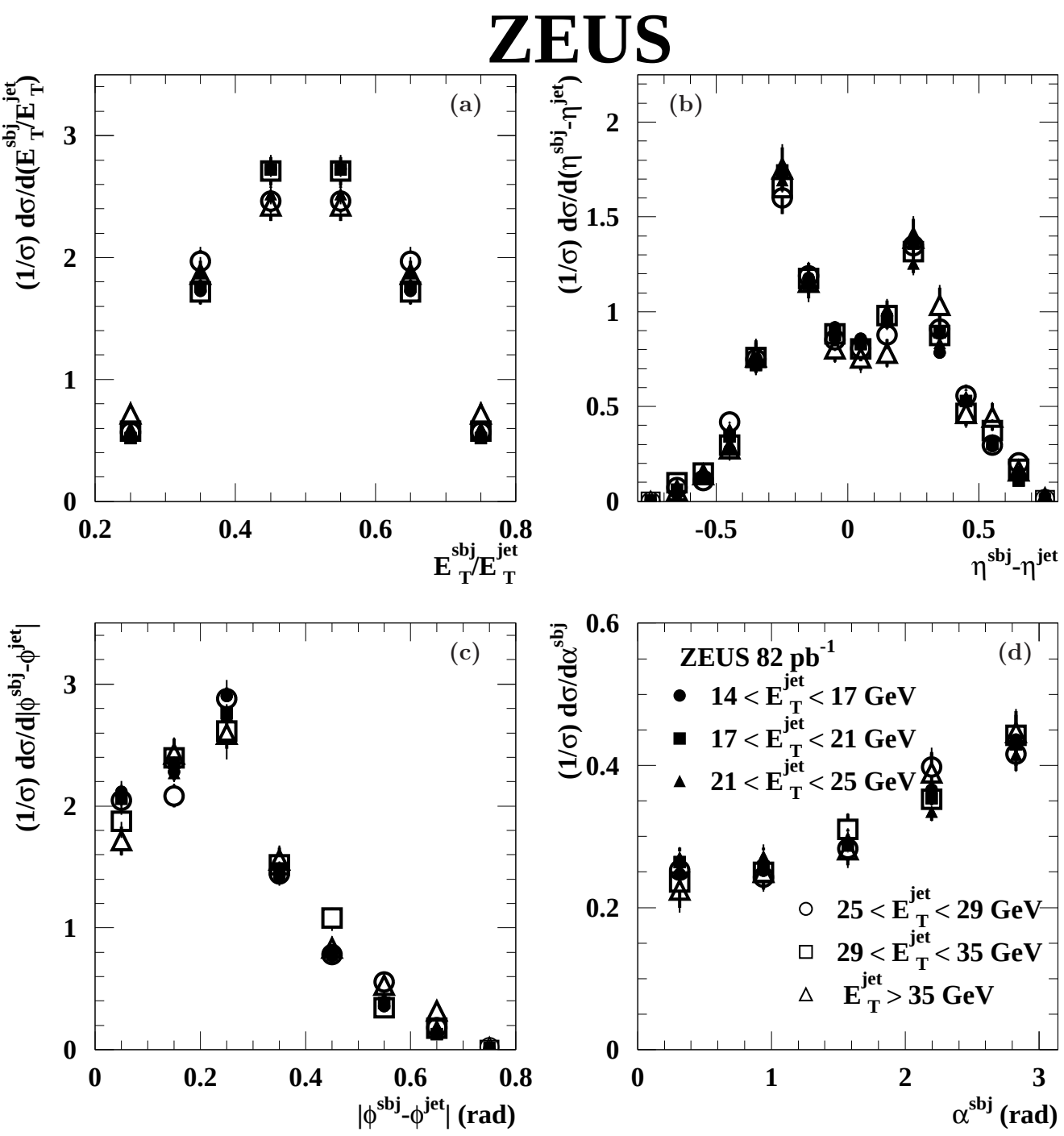

Figure 10: *Measured normalised differential subjet cross sections for jets with* $E_T^{\rm jet} > 14$ *GeV and* $-1 < \eta^{\rm jet} < 2.5$ *which have two subjets for* $y_{\rm cut} = 0.05$ *in the kinematic region given by* $Q^2 > 125$ *GeV*^{2} *as functions of (a)* $E_T^{\rm sbj}/E_T^{\rm jet}$*, (b)* $\eta^{\rm sbj} - \eta^{\rm jet}$*, (c)* $|\phi^{\rm sbj} - \phi^{\rm jet}|$ *and (d)* $\alpha^{\rm sbj}$ *in different regions of* $E_T^{\rm jet}$*. Details concerning the error bars are as in the caption to Fig. 3.*

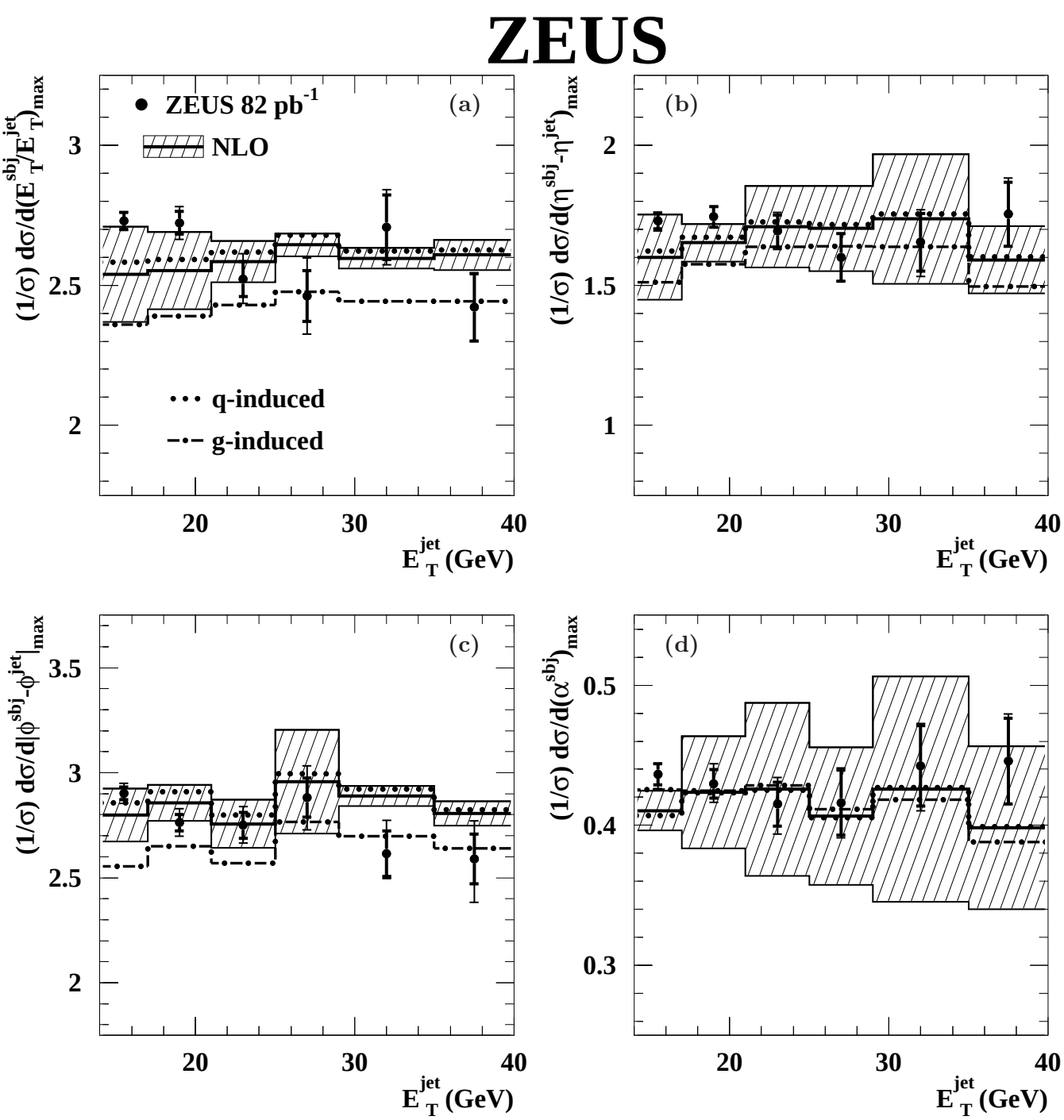

Figure 11: *Maximum of the measured normalised differential (a) $E_T^{\rm sbj}/E_T^{\rm jet}$, (b) $\eta^{\rm sbj} - \eta^{\rm jet}$, (c) $|\phi^{\rm sbj} - \phi^{\rm jet}|$ and (d) $\alpha^{\rm sbj}$ subjet cross sections (dots) for jets with $E_T^{\rm jet} > 14$ GeV and $-1 < \eta^{\rm jet} < 2.5$ which have two subjets for $y_{\rm cut} = 0.05$ in the kinematic region given by $Q^2 > 125$ GeV^2 as a function of $E_T^{\rm jet}$. For comparison, the NLO predictions for quark- (dotted histograms) and gluon-induced (dot-dashed histograms) processes are also shown separately. Other details are as in the caption to Fig. 3.*

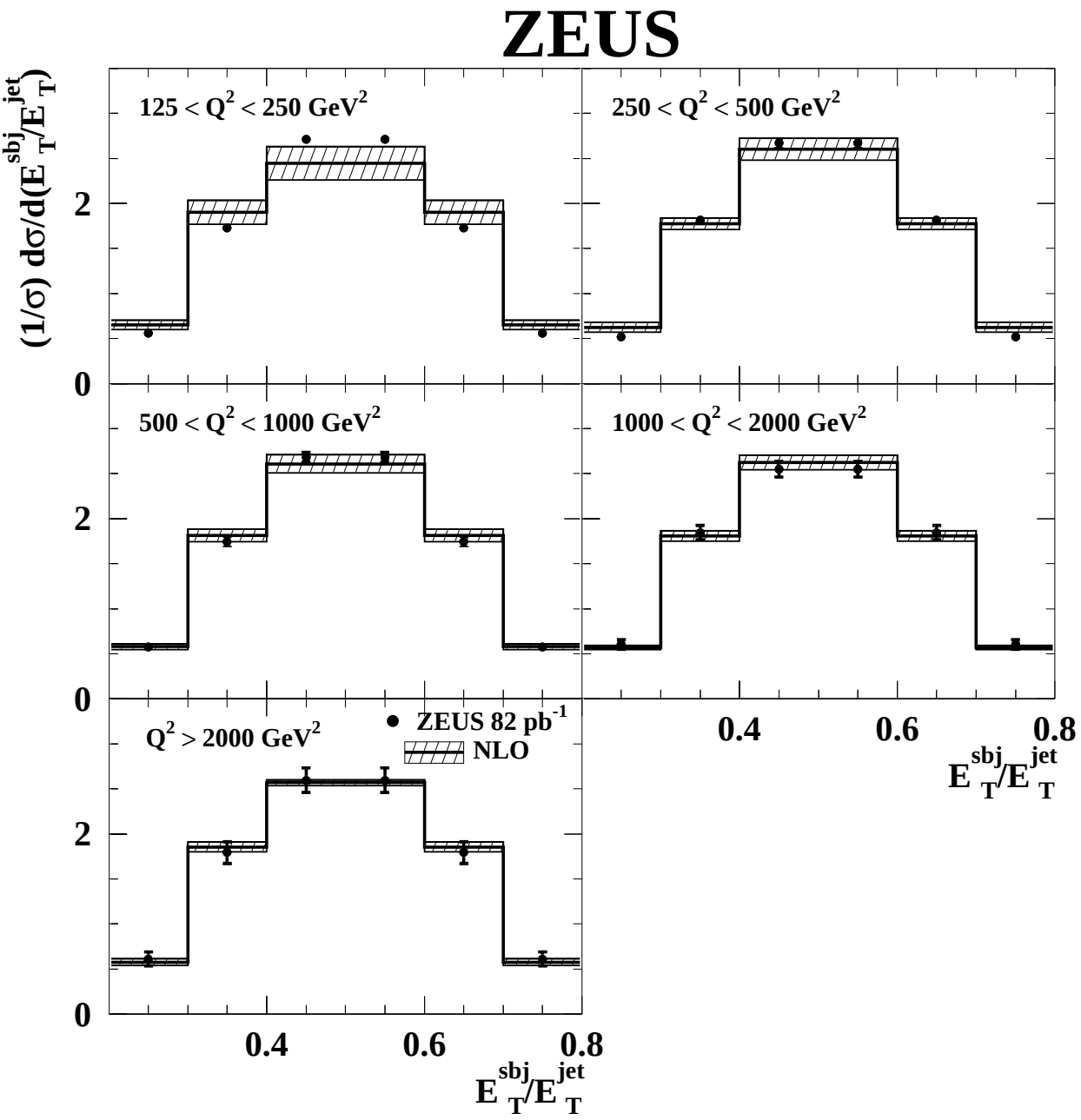

Figure 12: *Measured normalised differential subjet cross sections (dots) for jets with $E_T^{\rm jet} > 14$ GeV and $-1 < \eta^{\rm jet} < 2.5$ which have two subjets for $y_{\rm cut} = 0.05$ in the kinematic region given by $Q^2 > 125$ GeV^2 as functions of $E_T^{\rm sbj}/E_T^{\rm jet}$ in different regions of Q^2. Other details are as in the caption to Fig. 3.*

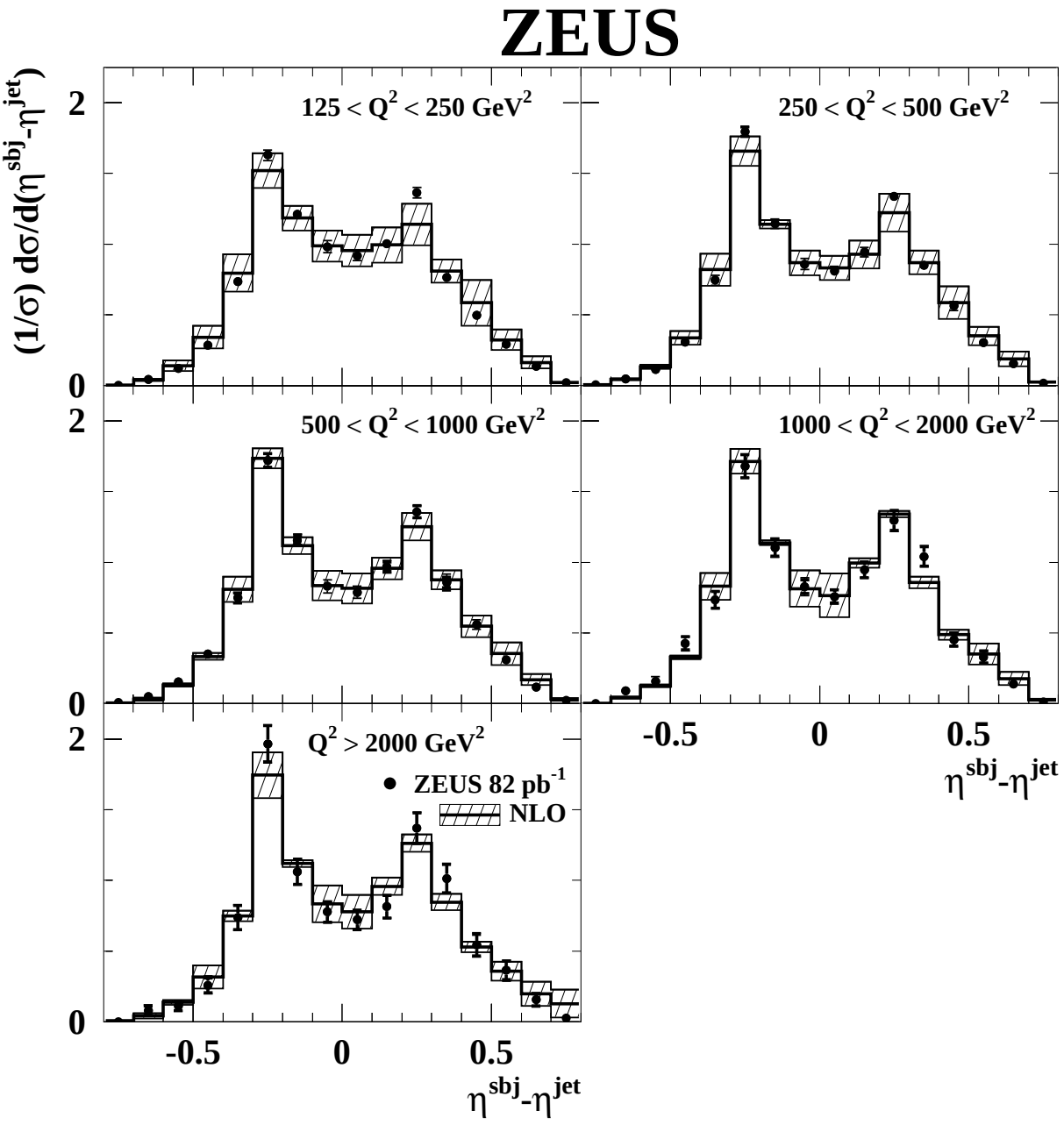

Figure 13: *Measured normalised differential subjet cross sections (dots) for jets with $E_T^{\rm jet} > 14$ GeV and $-1 < \eta^{\rm jet} < 2.5$ which have two subjets for $y_{\rm cut} = 0.05$ in the kinematic region given by $Q^2 > 125$ GeV^2 as functions of $\eta^{\rm sbj} - \eta^{\rm jet}$ in different regions of Q^2. Other details are as in the caption to Fig. 3.*

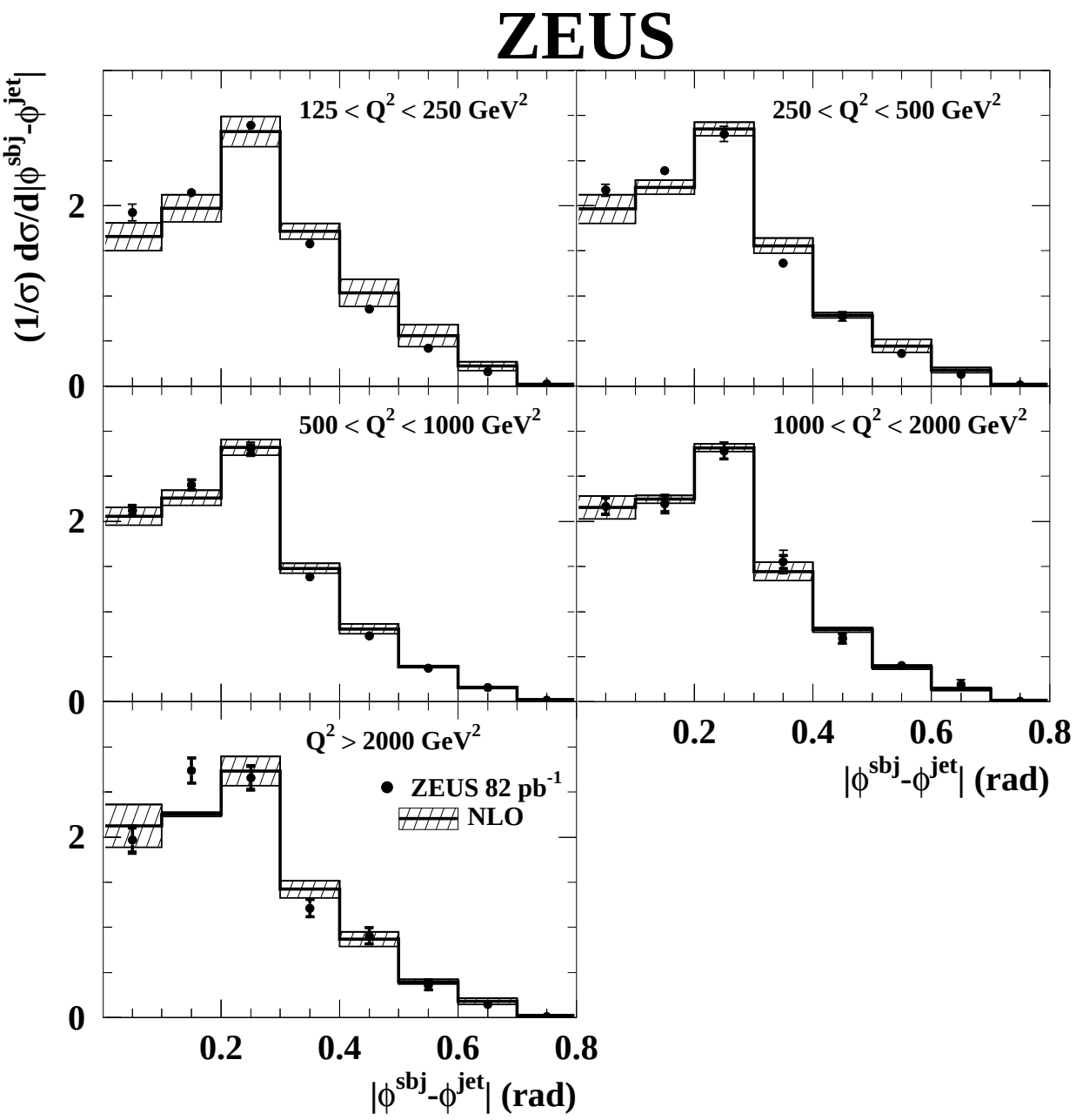

Figure 14: *Measured normalised differential subjet cross sections (dots) for jets with $E_T^{\rm jet} > 14$ GeV and $-1 < \eta^{\rm jet} < 2.5$ which have two subjets for $y_{\rm cut} = 0.05$ in the kinematic region given by $Q^2 > 125$ GeV^2 as functions of $|\phi^{\rm sbj} - \phi^{\rm jet}|$ in different regions of Q^2. Other details are as in the caption to Fig. 3.*

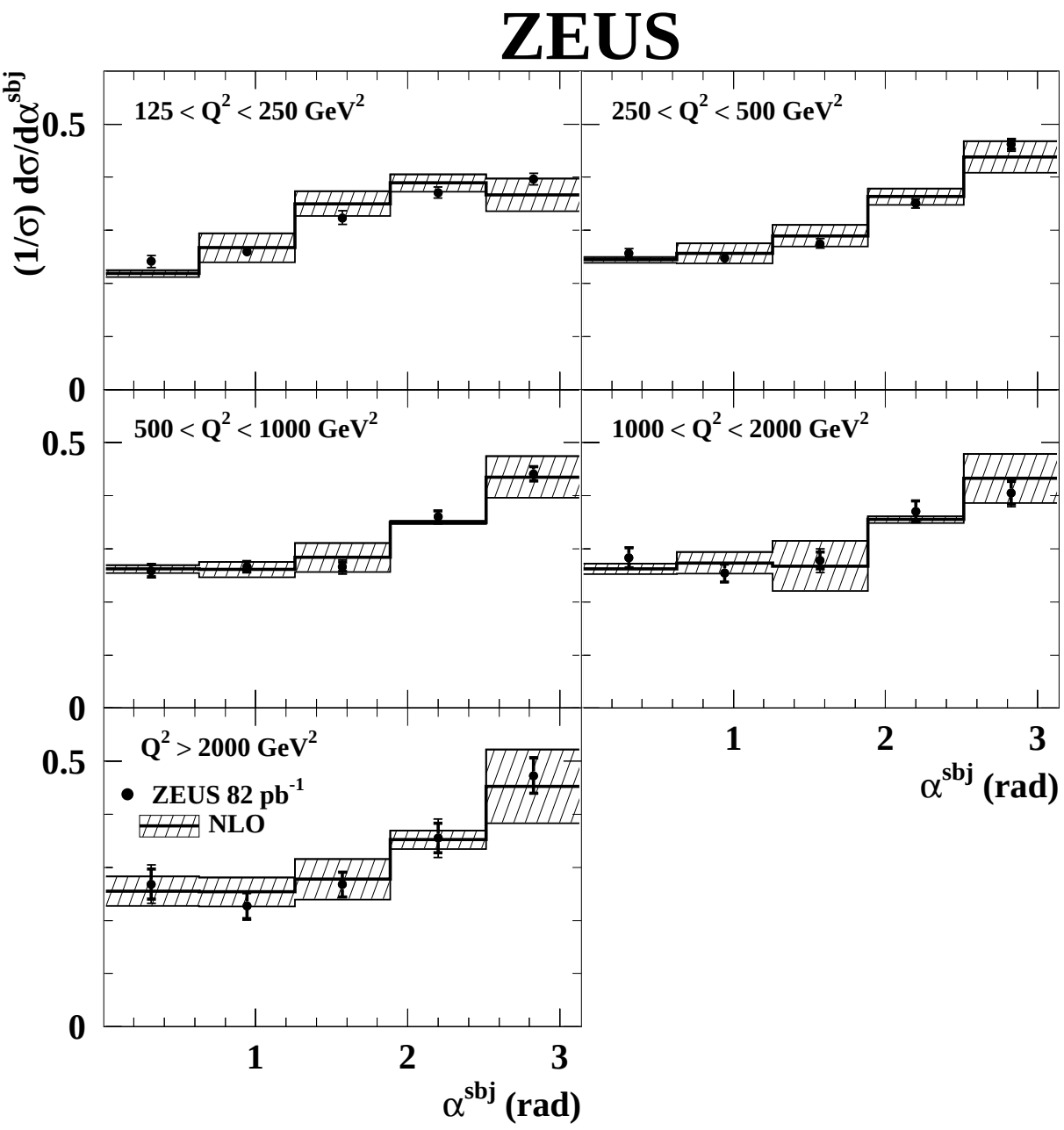

Figure 15: *Measured normalised differential subjet cross sections (dots) for jets with $E_T^{\rm jet} > 14$ GeV and $-1 < \eta^{\rm jet} < 2.5$ which have two subjets for $y_{\rm cut} = 0.05$ in the kinematic region given by $Q^2 > 125$ GeV^2 as functions of $\alpha^{\rm sbj}$ in different regions of Q^2. Other details are as in the caption to Fig. 3.*

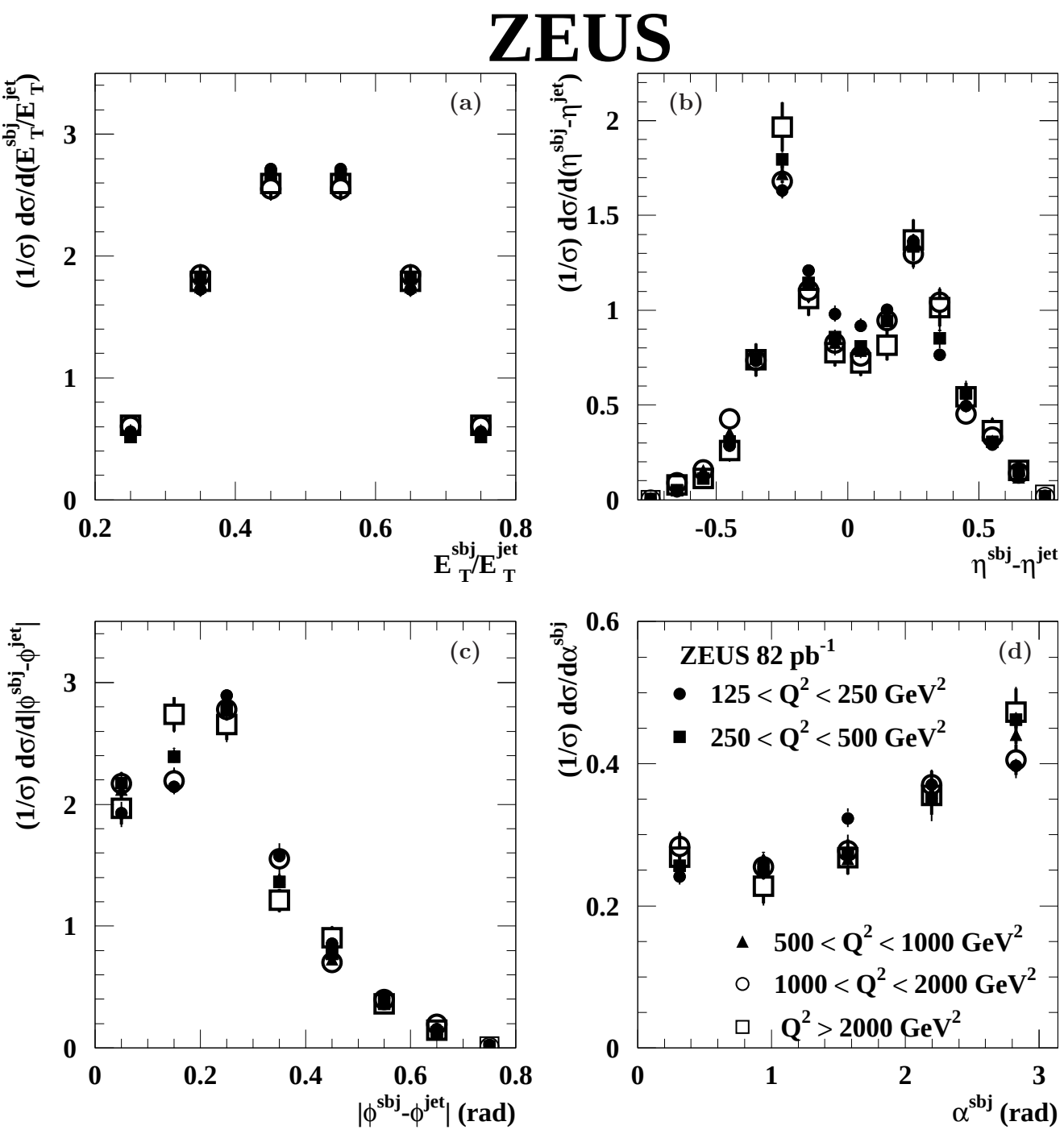

Figure 16: *Measured normalised differential subjet cross sections for jets with* $E_T^{\rm jet} > 14$ *GeV and* $-1 < \eta^{\rm jet} < 2.5$ *which have two subjets for* $y_{\rm cut} = 0.05$ *in the kinematic region given by* $Q^2 > 125$ *GeV*^{2} *as functions of (a)* $E_T^{\rm sbj}/E_T^{\rm jet}$*, (b)* $\eta^{\rm sbj} - \eta^{\rm jet}$*, (c)* $|\phi^{\rm sbj} - \phi^{\rm jet}|$ *and (d)* $\alpha^{\rm sbj}$ *in different regions of* Q^2*. Details concerning the error bars are as in the caption to Fig. 3.*

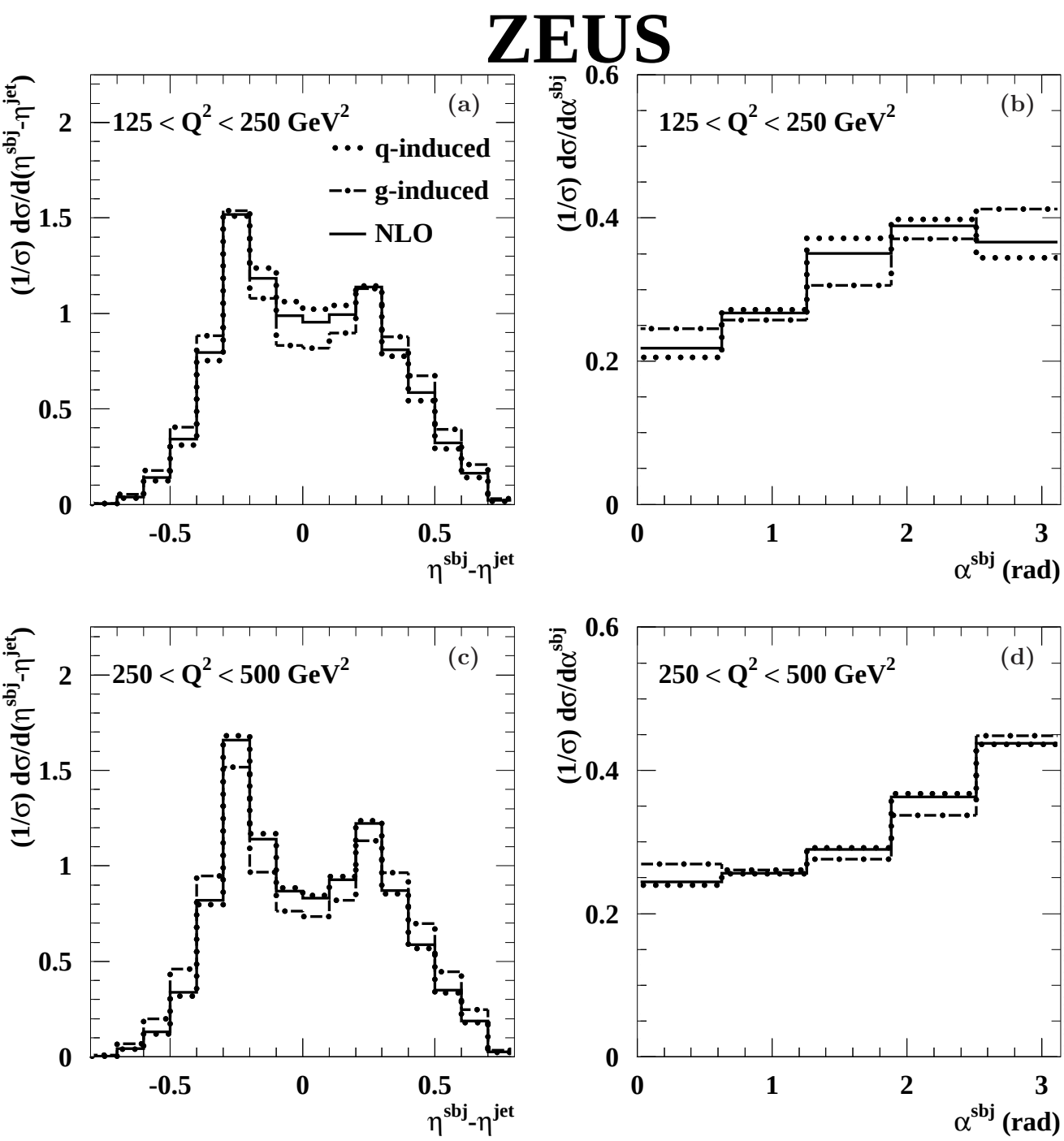

Figure 17: *Predicted normalised differential subjet cross sections (solid histograms) for jets with $E_T^{\rm jet} > 14$ GeV and $-1 < \eta^{\rm jet} < 2.5$ which have two subjets for $y_{\rm cut} = 0.05$ in the kinematic region given by $Q^2 > 125$ GeV^2 as functions of (a,c) $\eta^{\rm sbj} - \eta^{\rm jet}$ and (b,d) $\alpha^{\rm sbj}$ in different regions of Q^2. The NLO predictions for quark- (dotted histograms) and gluon-induced (dot-dashed histograms) processes are also shown separately.*

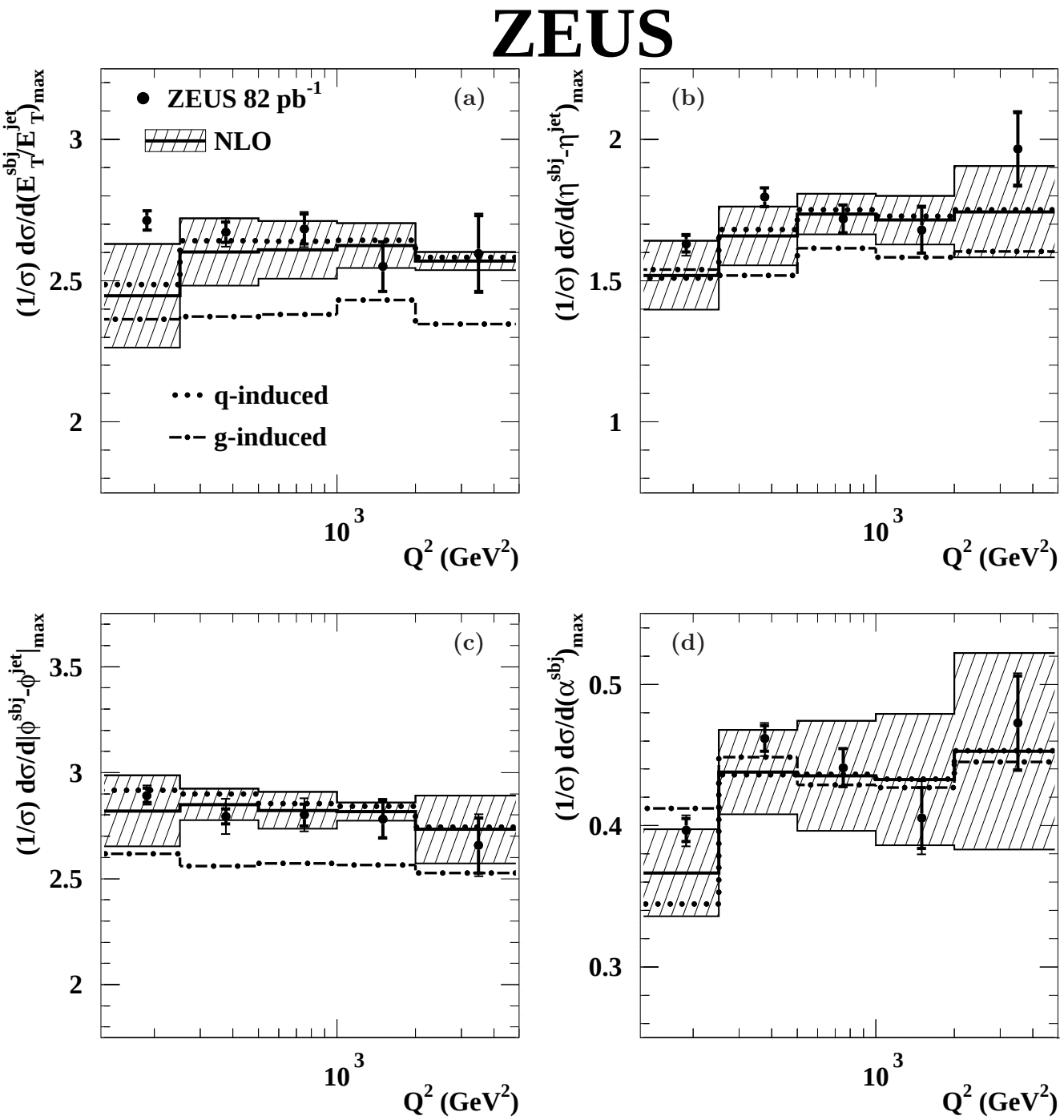

Figure 18: *Maximum of the measured normalised differential (a) $E_T^{\rm sbj}/E_T^{\rm jet}$, (b) $\eta^{\rm sbj}-\eta^{\rm jet}$, (c) $|\phi^{\rm sbj}-\phi^{\rm jet}|$ and (d) $\alpha^{\rm sbj}$ subjet cross sections (dots) for jets with $E_T^{\rm jet} > 14$ GeV and $-1 < \eta^{\rm jet} < 2.5$ which have two subjets for $y_{\rm cut} = 0.05$ in the kinematic region given by $Q^2 > 125$ GeV^2 as a function of Q^2. For comparison, the NLO predictions for quark- (dotted histograms) and gluon-induced (dot-dashed histograms) processes are also shown separately. Other details are as in the caption to Fig. 3.*

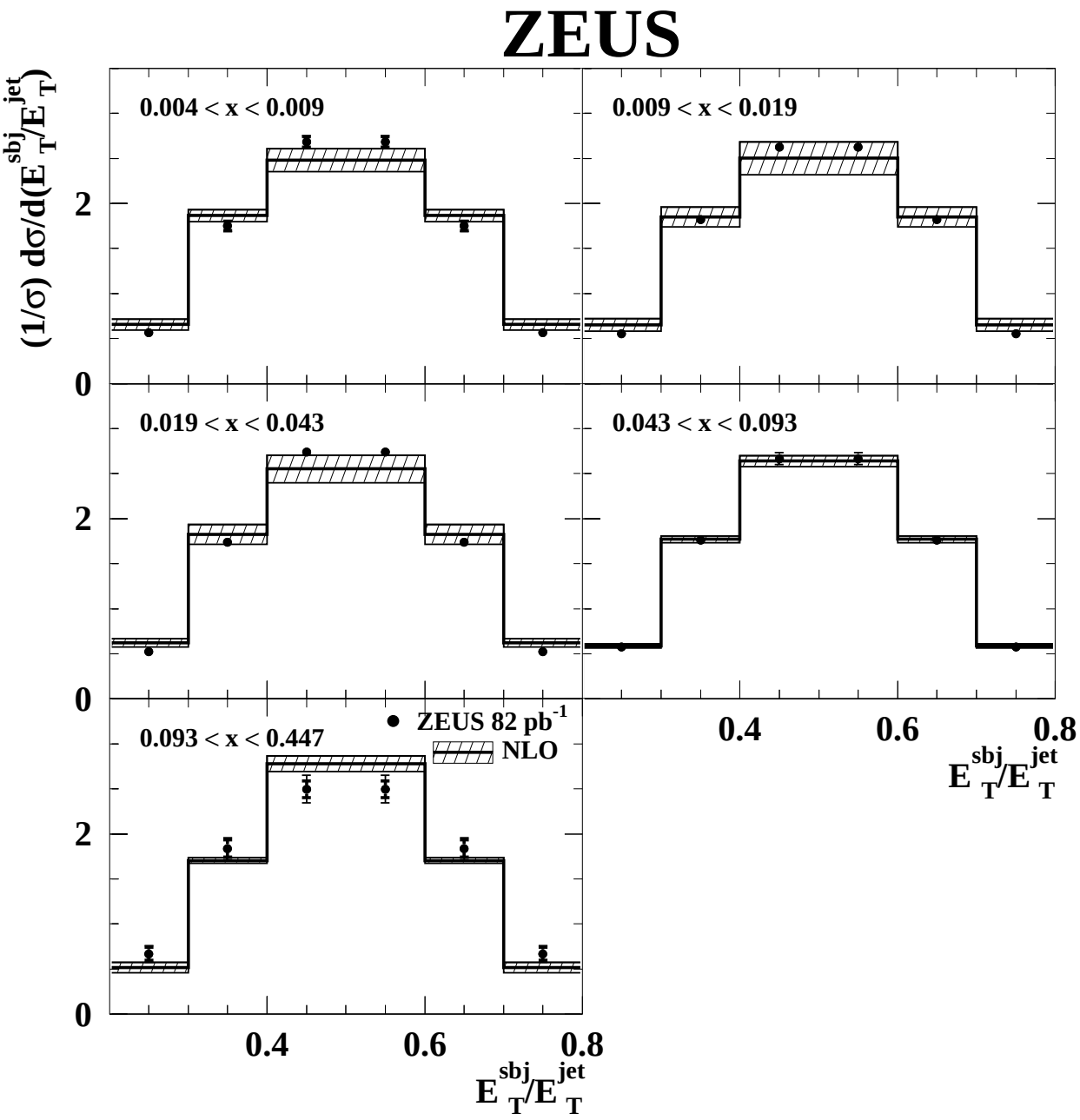

Figure 19: *Measured normalised differential subjet cross sections (dots) for jets with $E_T^{\rm jet} > 14$ GeV and $-1 < \eta^{\rm jet} < 2.5$ which have two subjets for $y_{\rm cut} = 0.05$ in the kinematic region given by $Q^2 > 125$ GeV^2 as functions of $E_T^{\rm sbj}/E_T^{\rm jet}$ in different regions of x. Other details are as in the caption to Fig. 3.*

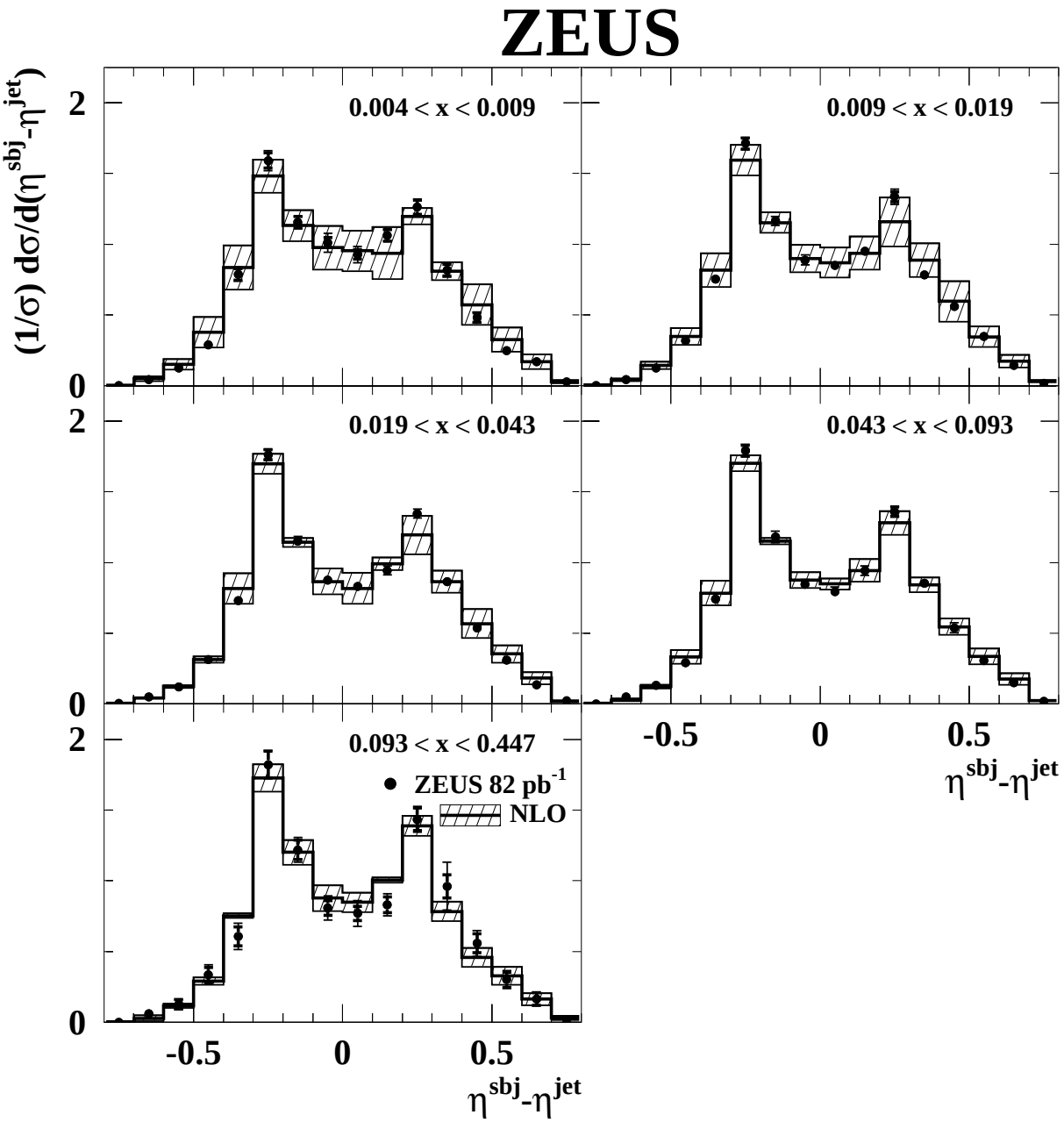

Figure 20: *Measured normalised differential subjet cross sections (dots) for jets with $E_T^{\rm jet} > 14$ GeV and $-1 < \eta^{\rm jet} < 2.5$ which have two subjets for $y_{\rm cut} = 0.05$ in the kinematic region given by $Q^2 > 125$ GeV^2 as functions of $\eta^{\rm sbj} - \eta^{\rm jet}$ in different regions of x. Other details are as in the caption to Fig. 3.*

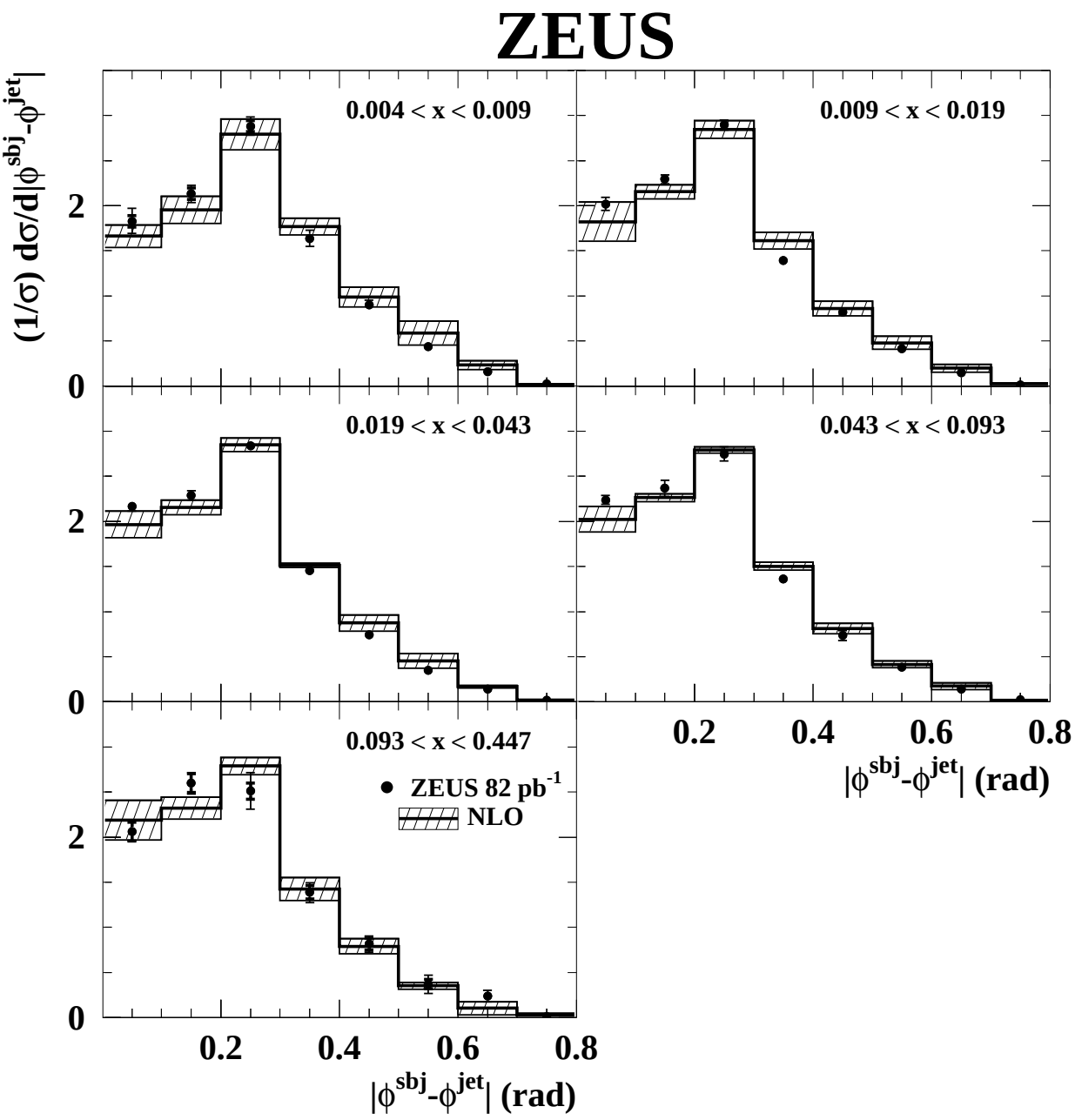

Figure 21: *Measured normalised differential subjet cross sections (dots) for jets with $E_T^{\rm jet} > 14$ GeV and $-1 < \eta^{\rm jet} < 2.5$ which have two subjets for $y_{\rm cut} = 0.05$ in the kinematic region given by $Q^2 > 125$ GeV^2 as functions of $|\phi^{\rm sbj} - \phi^{\rm jet}|$ in different regions of x. Other details are as in the caption to Fig. 3.*

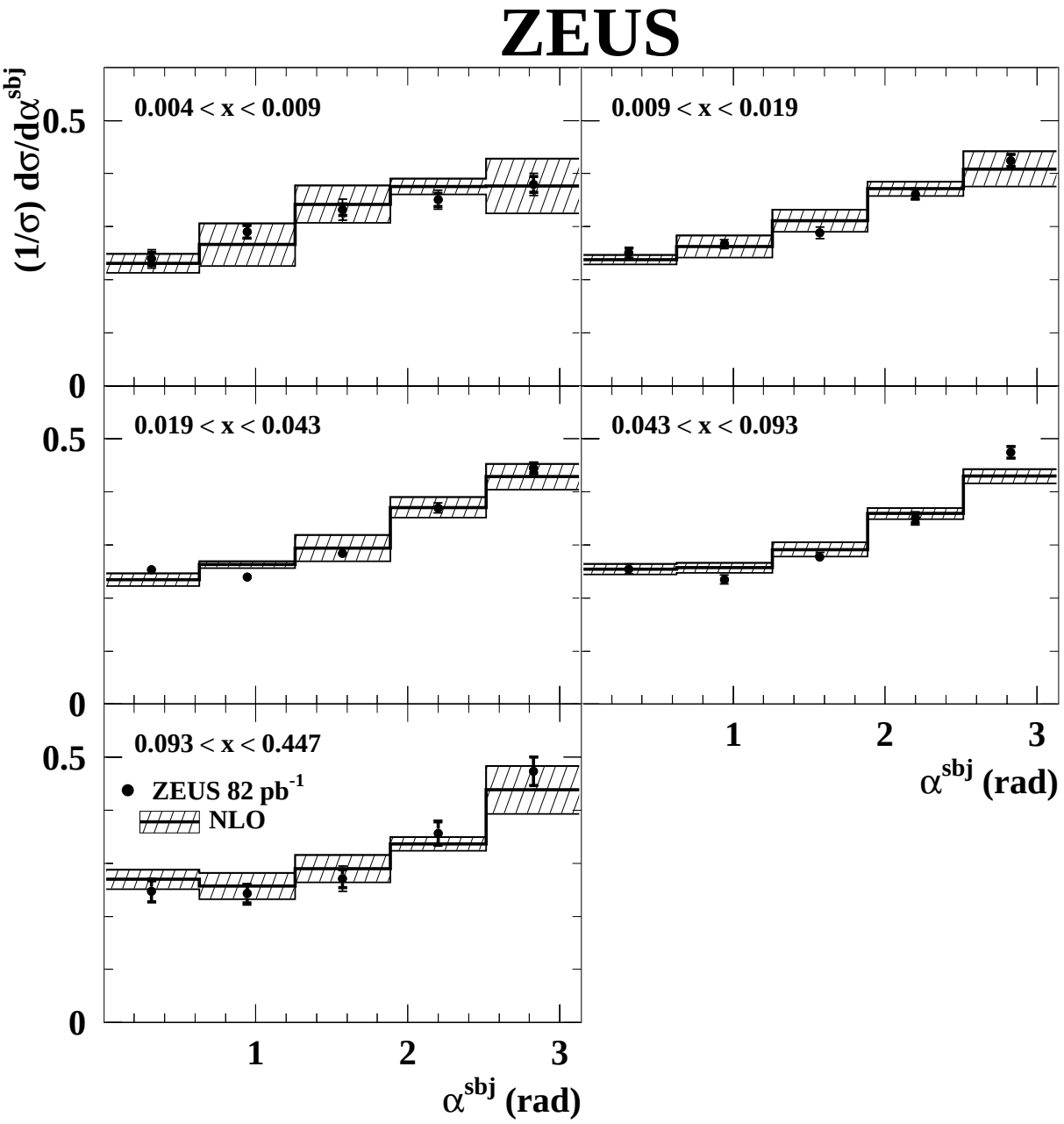

Figure 22: *Measured normalised differential subjet cross sections (dots) for jets with $E_T^{\rm jet} > 14$ GeV and $-1 < \eta^{\rm jet} < 2.5$ which have two subjets for $y_{\rm cut} = 0.05$ in the kinematic region given by $Q^2 > 125$ GeV^2 as functions of $\alpha^{\rm sbj}$ in different regions of x. Other details are as in the caption to Fig. 3.*

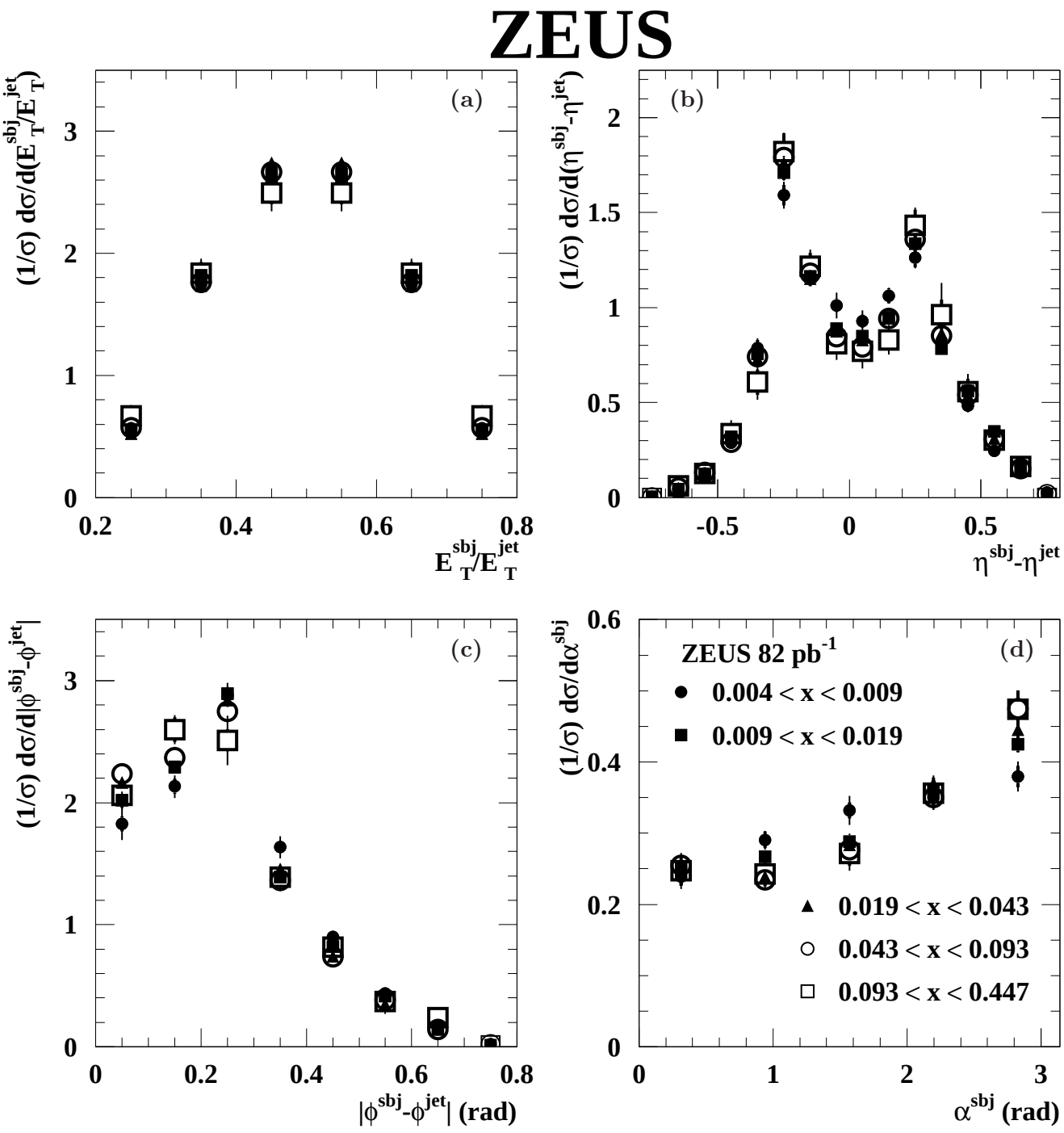

Figure 23: *Measured normalised differential subjet cross sections for jets with* $E_T^{\rm jet} > 14$ *GeV and* $-1 < \eta^{\rm jet} < 2.5$ *which have two subjets for* $y_{\rm cut} = 0.05$ *in the kinematic region given by* $Q^2 > 125$ *GeV*^{2} *as functions of (a)* $E_T^{\rm sbj}/E_T^{\rm jet}$*, (b)* $\eta^{\rm sbj} - \eta^{\rm jet}$*, (c)* $|\phi^{\rm sbj} - \phi^{\rm jet}|$ *and (d)* $\alpha^{\rm sbj}$ *in different regions of* x*. Details concerning the error bars are as in the caption to Fig. 3.*

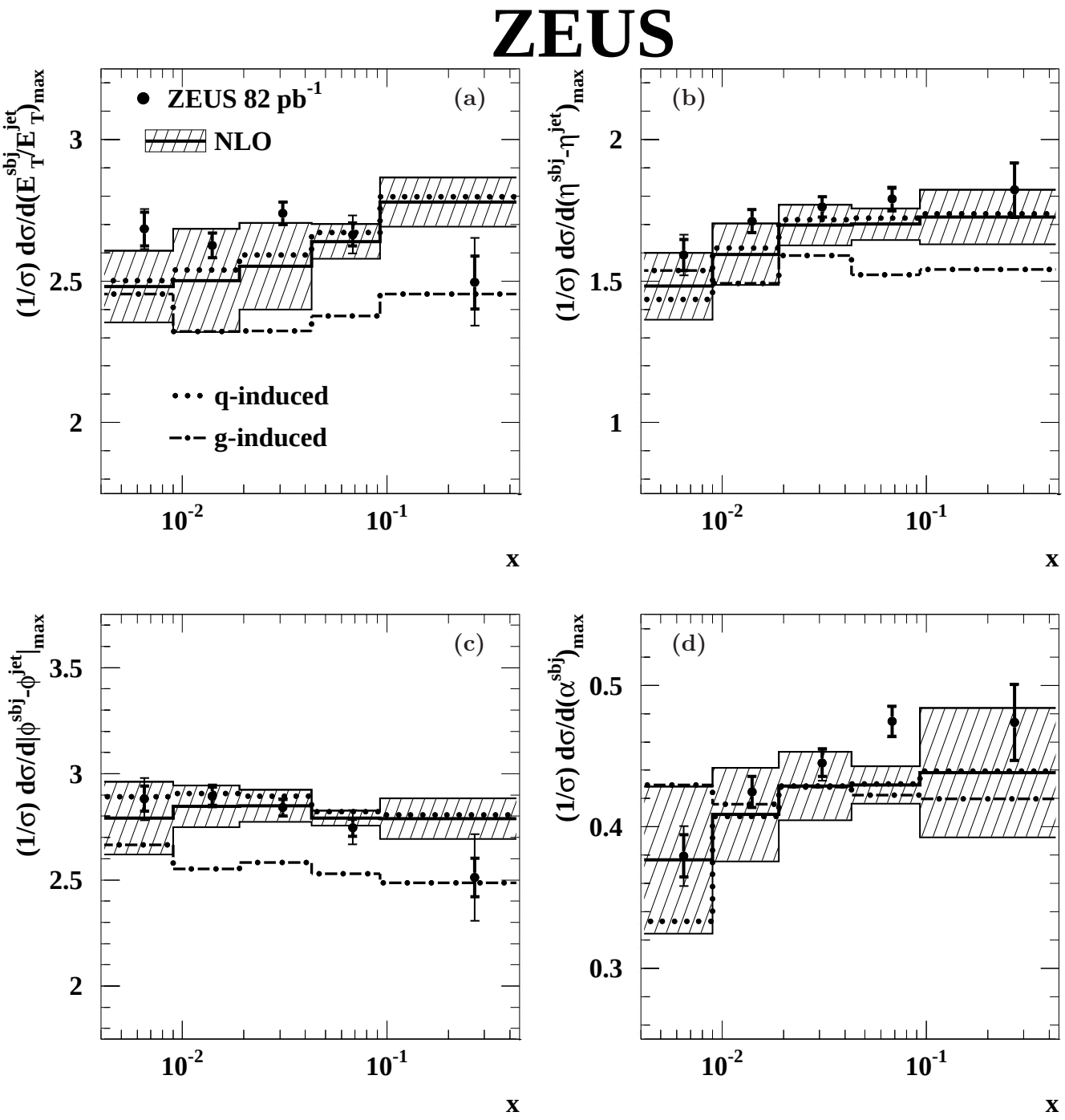

Figure 24: *Maximum of the measured normalised differential (a) $E_T^{\rm sbj}/E_T^{\rm jet}$, (b) $\eta^{\rm sbj}-\eta^{\rm jet}$, (c) $|\phi^{\rm sbj}-\phi^{\rm jet}|$ and (d) $\alpha^{\rm sbj}$ subjet cross sections (dots) for jets with $E_T^{\rm jet} > 14$ GeV and $-1 < \eta^{\rm jet} < 2.5$ which have two subjets for $y_{\rm cut} = 0.05$ in the kinematic region given by $Q^2 > 125$ GeV^2 as a function of x. For comparison, the NLO predictions for quark- (dotted histograms) and gluon-induced (dot-dashed histograms) processes are also shown separately. Other details are as in the caption to Fig. 3.*

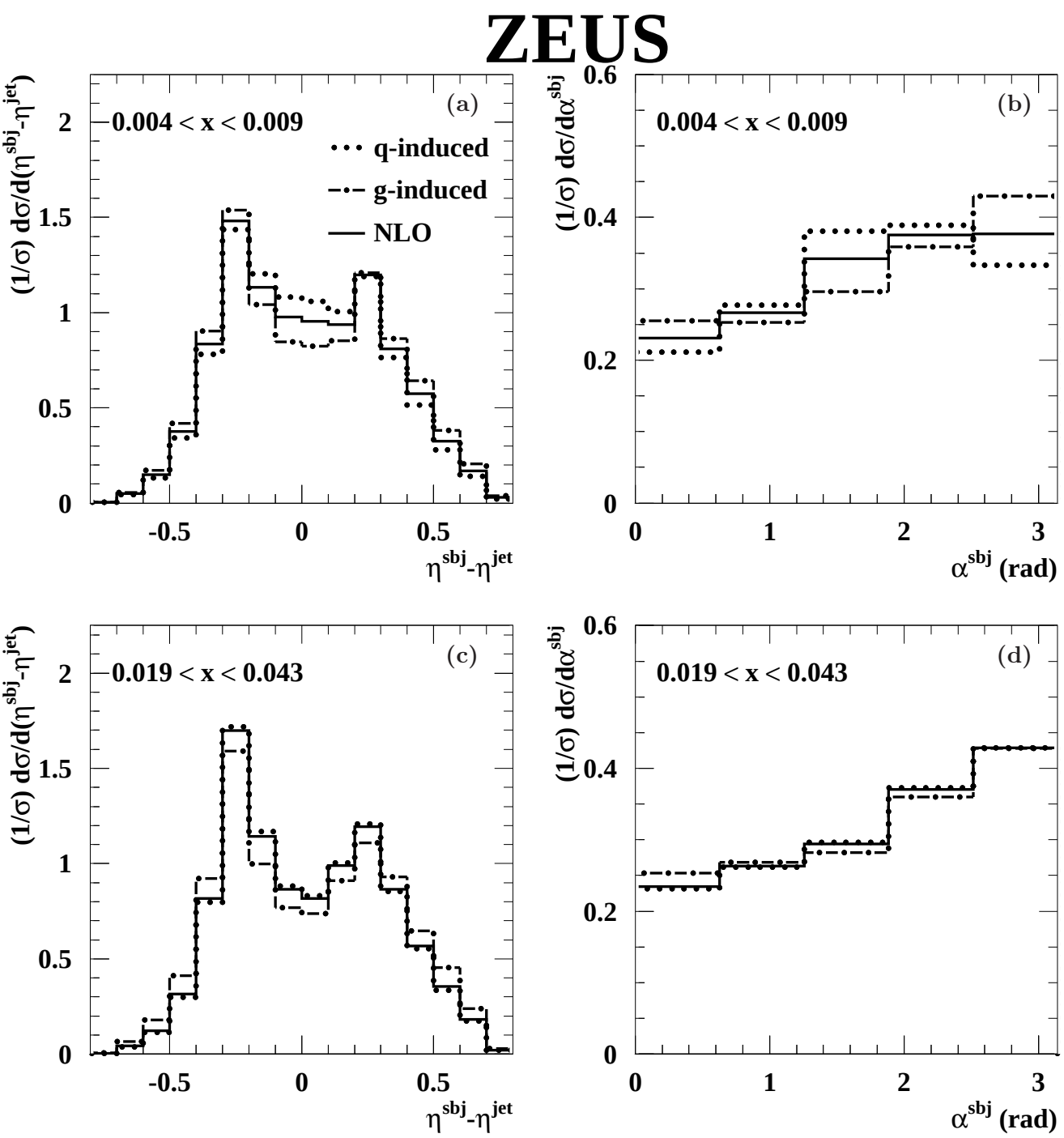

Figure 25: *Predicted normalised differential subjet cross sections (solid histograms) for jets with $E_T^{\rm jet} > 14$ GeV and $-1 < \eta^{\rm jet} < 2.5$ which have two subjets for $y_{\rm cut} = 0.05$ in the kinematic region given by $Q^2 > 125$ GeV^2 as functions of (a,c) $\eta^{\rm sbj} - \eta^{\rm jet}$ and (b,d) $\alpha^{\rm sbj}$ in different regions of x. The NLO predictions for quark- (dotted histograms) and gluon-induced (dot-dashed histograms) processes are also shown separately.*

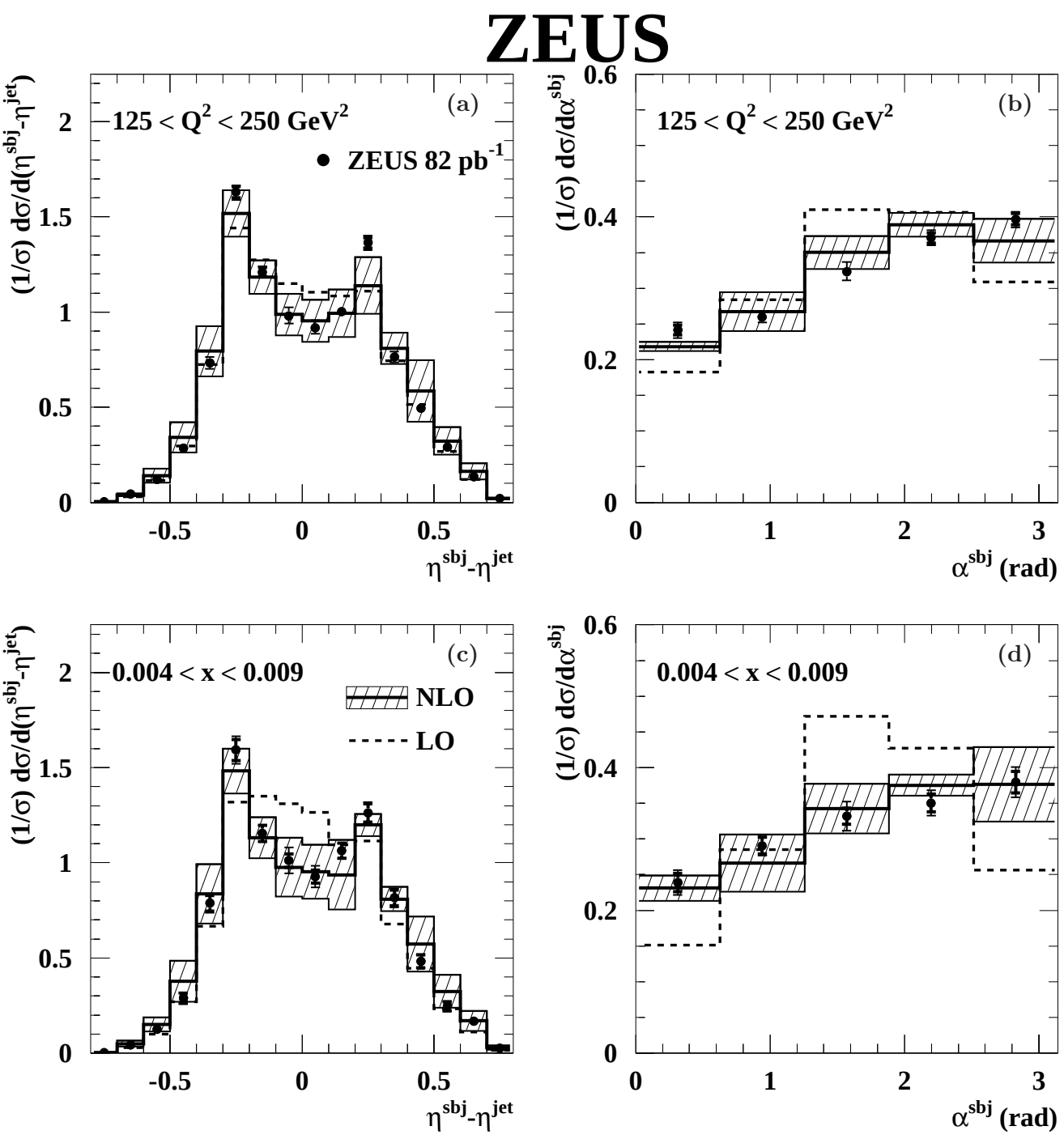

Figure 26: *Measured normalised differential subjet cross sections (dots) for jets with $E_T^{\rm jet} > 14$ GeV and $-1 < \eta^{\rm jet} < 2.5$ which have two subjets for $y_{\rm cut} = 0.05$ in restricted Q^2 and x regions as functions of (a,c) $\eta^{\rm sbj} - \eta^{\rm jet}$ and (b,d) $\alpha^{\rm sbj}$. The NLO (solid histograms) and LO (dashed histograms) calculations are also shown. The hatched bands represent the NLO theoretical uncertainty.*